JOURNAL OF PETROLOGY | VOLUME 38 | NUMBER 6 | PAGES 757–783 | 1997

# Mineral Zoning, *P–T–X–M* Phase Relations, and Metamorphic Evolution of some Adirondack Granulites, New York*

**FRANK S. SPEAR† AND JEFFREY C. MARKUSSEN**

DEPARTMENT OF EARTH AND ENVIRONMENTAL SCIENCE, RENSSELAER POLYTECHNIC INSTITUTE, TROY, NY 12180, USA

*Detailed petrologic analysis of ten meta-anorthosites and related rocks from the Adirondack highlands, New York, has been used to constrain the* P–T *history of the region. Metamorphic orthopyroxene and clinopyroxene occur in aggregates of ~1 mm diameter grains that are zoned concentrically with decreasing Al and Fe/(Fe+Mg) and increasing Ca towards the rim; moreover, zoning is not related to the presence of garnet. Zoning is interpreted to have been produced during growth by the reaction: igneous pyroxene+plagioclase= metamorphic Opx+metamorphic Cpx along a cooling path with a slope of 6 bars/°C starting at ~850°C and 6·5–8 kbar. Garnet occurs as isolated clusters of 5–25 grains of ~1 mm diameter crystals and as necklaces of ~1 mm diameter crystals surrounding metamorphic pyroxenes or oxides. Plagioclase±quartz typically separates garnet from pyroxene, but locally garnet embays metamorphic pyroxene, suggesting that garnet grew at the expense of pyroxene. Garnet clusters have slightly lower Fe/(Fe+Mg) than garnet in necklaces [Fe/(Fe+Mg)=0·73 and 0·75–0·78, respectively] and slightly higher grossular ($X_{grs}$=0·20 vs 0·19). Neither is zoned in Mn and zoning towards increasing Fe/(Fe+Mg) is restricted to contacts with biotite and locally clinopyroxene. Biotite adjacent to garnet is zoned towards decreasing Fe/(Fe+Mg). Production of garnet in necklaces is interpreted to be the result of the continuous Fe–Mg reaction Opx+Pl= Grt+Cpx+Qtz.* P–T–X–M *modeling of this reaction reveals a* P–T *path with a slope of 6 bars/°C. No evidence for early, pre-metamorphic peak garnet is observed, which rules out any possibility of early higher-pressure metamorphism. The* P–T *path is therefore inferred to be counterclockwise with loading to 6·5–8 kbar at a maximum temperature of ~850°C occurring during or immediately following an influx of heat, presumably from early orogenic plutons.*

KEY WORDS: *Adirondacks; granulites;* P–T *paths; garnet zoning; Gibbs method*

## INTRODUCTION

The Adirondack highlands of New York are one of the best studied granulite facies terranes of the world (e.g. Bohlen *et al.*, 1985; Valley *et al.*, 1990, and references therein). Based on this considerable volume of work, the peak metamorphic conditions in the Adirondack highlands have been fairly well constrained at pressures of ~7–8 kbar (crustal depths of 25–30 km) and temperatures that range from >775°C in the central highlands to $T$<675°C in the southern Adirondacks (e.g. Bohlen *et al.*, 1985). *P–T* paths have been shown to follow nearly isobaric cooling trajectories (e.g. Bohlen, 1987). Because of this wealth of information, some fundamental questions about the origin of the Adirondack granulite facies terrane have emerged (e.g. Bohlen *et al.*, 1985): How did the crust achieve the relatively high temperature conditions necessary to produce granulite facies rocks at depths of 25–30 km? And what is the relative importance of magmatic heating vs continental burial in this process?

This study will present new data on mineral composition and element zoning in garnet, pyroxene, biotite, amphibole and plagioclase from Adirondack meta-anorthosite and related rocks with the goal of further constraining the metamorphic evolution of this terrane. Mineral compositions will be used to construct phase diagrams in an attempt to evaluate approach to chemical equilibrium. Theoretical analysis will be used to construct *P–T–X–M* phase diagrams depicting how mineral composition and modes change with $P$ and $T$. This theoretical analysis will then be applied to the mineral zoning to constrain the *P–T* path, and the results will be discussed in the context of a tectonic model for the Adirondacks.

*Color images and tiff files to download are available at http://www.geo.rpi.edu/facstaff/spear/adk/adk.html

†Corresponding author.

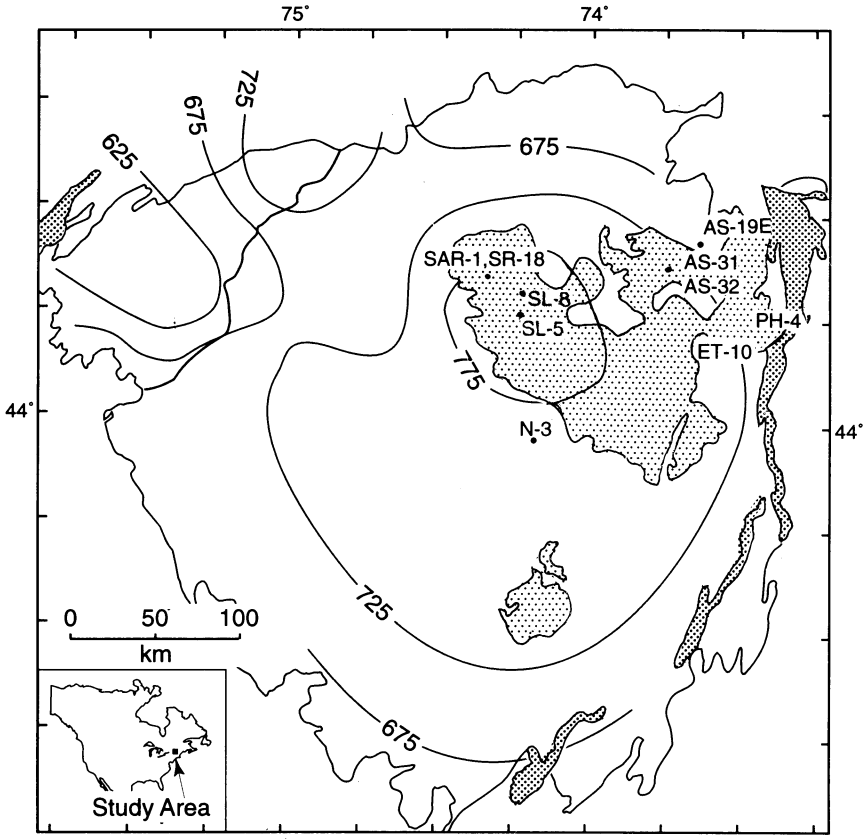


**Fig. 1.** Map of the Adirondack mountains, NY, showing location of samples examined in this study. Light gray shading delineates the outcrop exposure of the anorthosite [after McLelland & Chiarenzelli (1990)]; surrounding rocks are ortho- and paragneisses of diverse affinities; darker gray is water. Contours show isotherms of temperature calculated from feldspar and oxide thermometry by Bohlen *et al.* (1980, 1985).

## GEOLOGIC SETTING

Figure 1 shows a map of the Adirondack mountains depicting the locations of samples analyzed in this study. Of the ten samples selected for detailed analysis, eight are meta-anorthosite (ET-10, PH-4, AS-31, AS-32, SAR-1, SR-18, SL-8, and SL-5), one is from the Lyon Mt. Gneiss (AS-19E) and one is a two-pyroxene + garnet + hornblende + biotite granulite of unknown protolith (N3). Also shown in Fig. 1 are isotherms of central Adirondack peak metamorphic temperatures, determined from two-feldspar and Fe–Ti oxide thermometry (Bohlen *et al.*, 1980, 1985). Three of the samples come from areas below the 725°C isotherm (ET-10, PH-4, AS-19E), three come from areas between the 725 and 775°C isotherms (AS-31, AS-32, N-3), and four come from areas above the 775°C isotherm (SAR-1, SR-18, SL-8, SL-5)

## REACTION TEXTURES AND COMPOSITIONAL ZONING

Details of the petrography and mineral zoning from three samples (ET-10, AS-31 and SAR-1) are presented in Figs 2–8. Each sample contains igneous plagioclase, metamorphic plagioclase, K-feldspar, relict igneous clino- and/or orthopyroxene, metamorphic clino- and orthopyroxene, garnet, oxides (ilmenite ± magnetite) ± biotite ± hornblende. The samples differ in features such as the nature of plagioclase recrystallization and zoning, the texture of the metamorphic garnet, and the degree to which oxide is involved in metamorphic reaction.

An important inference to draw from examination of compositional zoning is whether the zoning is the product of growth processes, or whether zoning has been substantially modified by diffusion. These issues will be addressed in each of the samples as they are discussed.

### AS-31

Sample AS-31 (Figs 2 and 3) contains relict pigeonite megacrysts surrounded by a reaction zone of metamorphic clinopyroxene, minor metamorphic orthopyroxene plus small amounts of plagioclase, biotite and hornblende. The distinctive feature of AS-31 is the

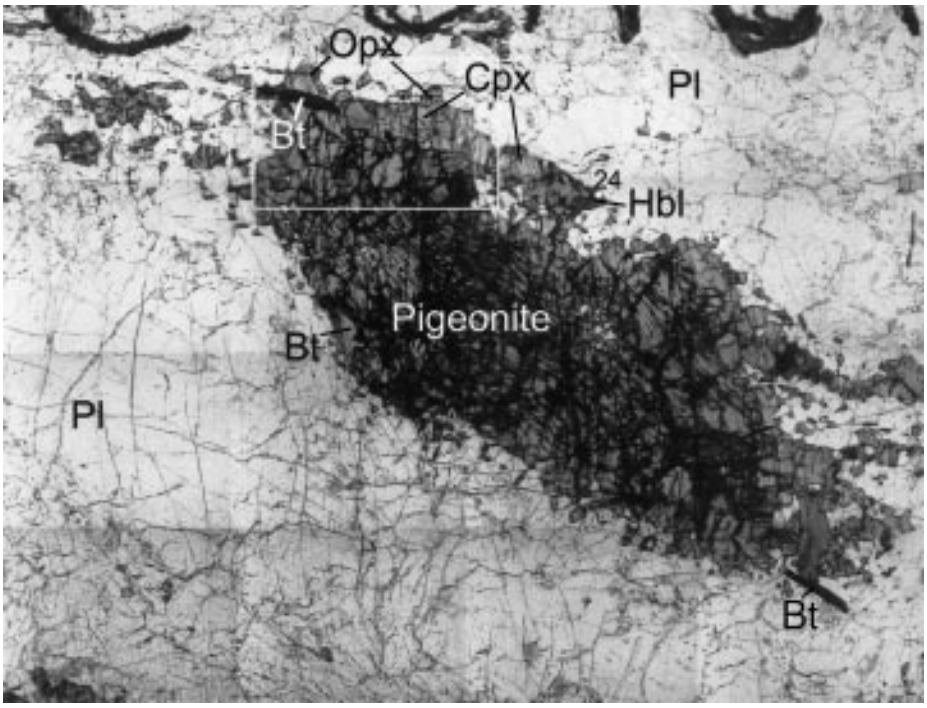


**Fig. 2.** Photomicrograph of pigeonite megacryst from sample AS-31. (Note reaction rim of clinopyroxene and orthopyroxene along top margin of crystal and crystals of biotite and hornblende at the margin of the pyroxene cluster.) Matrix is plagioclase. Box shows location of photomicrograph in Fig. 3a. Width of field is 17 mm. Number indicates location of analysis in Table 1.

absence of garnet in the thin section (although a single 1 mm crystal was observed in the thin section chip). Therefore, reactions and zoning observed in this sample must be attributed to reactions that do not involve garnet. Sample AS-31 is one of the most Mg-rich samples in the suite (based on Fe/Mg of pyroxene), which, as will be discussed later, accounts for the absence of garnet.

Zoning in clinopyroxene (Fig. 3d–f) is characterized by core-to-rim decreases in Al and Fe/(Fe + Mg) and an increase in Ca. Significantly, the zoning is symmetric within each pyroxene, suggesting that the zoning is the product of growth processes. Variations in Na (not shown) are <0·01 cation/6 oxygens and are patchy rather than symmetric from core to rim, suggesting these variations are not the result of growth processes. Although variations in Al and Fe/(Fe + Mg) also exist in orthopyroxene, the core-to-rim pattern is not evident (Fig. 3b). Plagioclase is also zoned (Fig. 3c), with An content ranging from $An_{51}$ in plagioclase core to $An_{67}$ where in contact with pyroxene.

## ET-10

Sample ET-10 (Figs 4–6) contains ortho- and clinopyroxene megacrysts, plagioclase, K-feldspar, metamorphic ortho- and clinopyroxene, garnet, biotite, oxides and a trace of hornblende. Metamorphic pyroxenes occur exclusively surrounding pyroxene megacrysts and comprise numerous small (0·5–2 mm diameter) crystals (Figs 4 and 5). Distinctive in this sample is the occurrence of garnet in two habits: (1) clusters of crystals either isolated from or adjacent to pyroxenes (lower left corner of Fig. 4); (2) necklaces of garnet that occur exclusively on the border between pyroxene aggregates and plagioclase (see Figs 4–6).

Figure 5a shows a detail of a garnet necklace adjacent to metamorphic clinopyroxene. Metamorphic clinopyroxenes are zoned in Al and Fe/(Fe + Mg) (Fig. 5d and e) with core-to-rim variations in Al of 0·15–0·11 (cations/6 oxygens) and in Fe/(Fe + Mg) of 0·39–0·33. This zoning is roughly concentric around each pyroxene grain, and not monotonic towards the garnet necklace, suggesting that at least some of the zoning is probably not associated with the garnet-producing reaction, but rather predates garnet growth, similar to sample AS-31. However, it is also possible that fast grain boundary diffusion along Cpx–Cpx grain boundaries imposes compositional gradients at the rim of each individual clinopyroxene grain, which could then develop into compositional zoning by diffusive processes. The similarity of the zoning in this sample to that in sample AS-31, which contains negligible garnet, suggests that at least some of the Al and Fe/(Fe + Mg) zoning in the clinopyroxene results from pre-garnet growth processes.

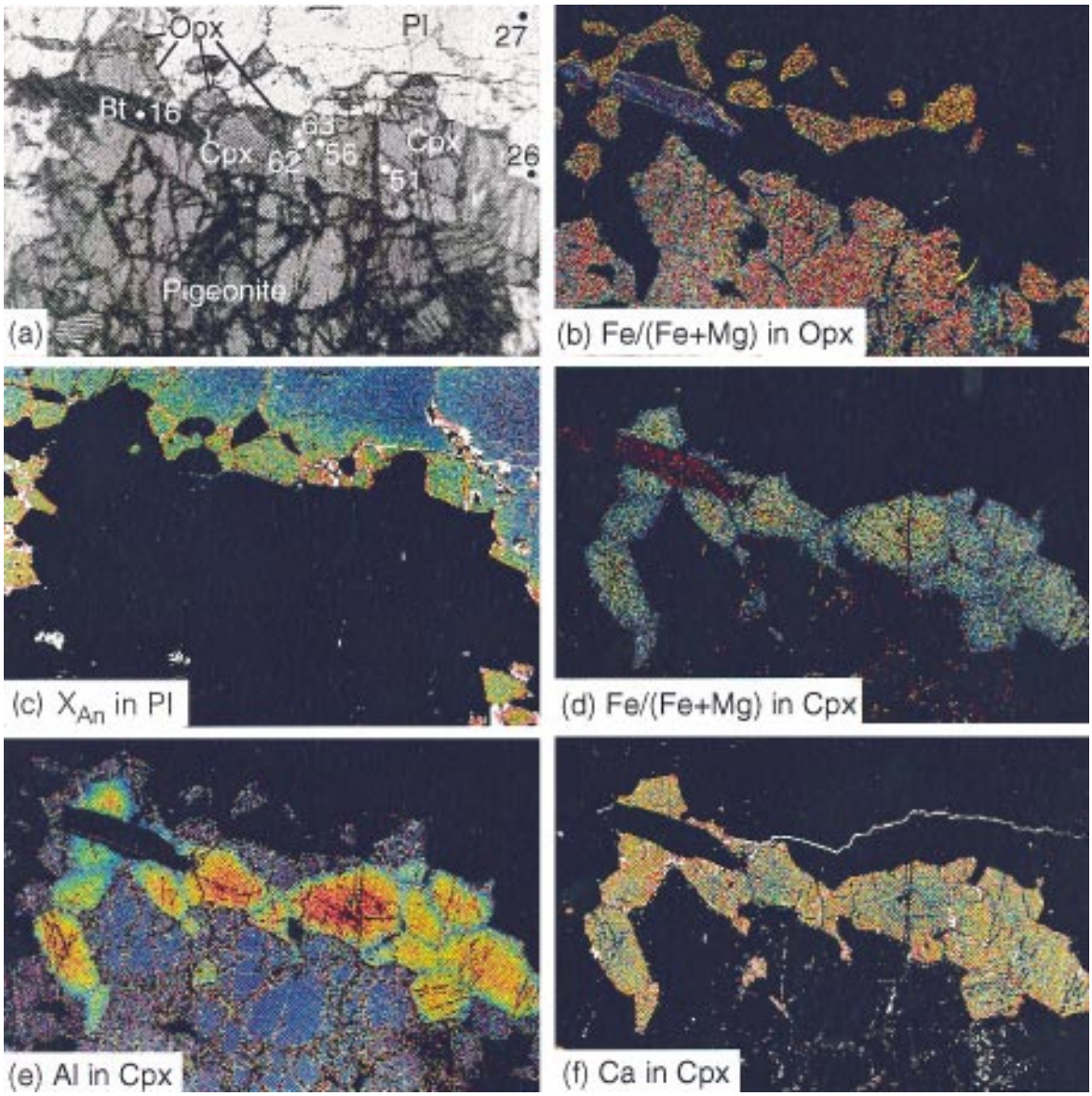


**Fig. 3.** Photomicrograph (a) and X-ray composition maps (b–f) from sample AS-31. (b) Fe/(Fe+Mg) in orthopyroxene; (c) $X_{An}$ in plagioclase; (d) Fe/(Fe+Mg) in clinopyroxene; (e) Al in clinopyroxene; (f) Ca in clinopyroxene. Warm colors are high values, cool colors are low values. [Note the core-to-rim decrease in Al and Fe/(Fe+Mg) and increase in Ca in clinopyroxene and the absence of systematic Fe/(Fe+Mg) zoning in orthopyroxene.] Plagioclase shows increase in $X_{An}$ towards the reaction zone. Field of view in (a) is 4·4 mm. Numbers indicate location of analyses in Table 1. Color images of all X-ray maps and tiff files to download are available at http://www.geo.rpi.edu/facstaff/spear/adk/adk.html

Clinopyroxene is also zoned in Ca with core-to-rim increases of 0·85–0·91 (cations/6 oxygens) (Fig. 5f). Variations in Na are <0·01 cations/6 oxygens and display no systematic trends.

Garnet is zoned in Fe/(Fe+Mg) along some contacts with clinopyroxene (Fig. 5b). The asymmetry of this zoning towards clinopyroxene suggests that it might be the result of diffusion driven by Fe–Mg exchange between garnet and clinopyroxene during cooling. However, not all garnet–clinopyroxene contacts show this zoning (a notable example is the garnet–clinopyroxene contact in the upper right quadrant of Fig. 6b). Therefore, it is concluded that this zoning is actually the result of garnet growth by continuous reaction. Very minor concentric

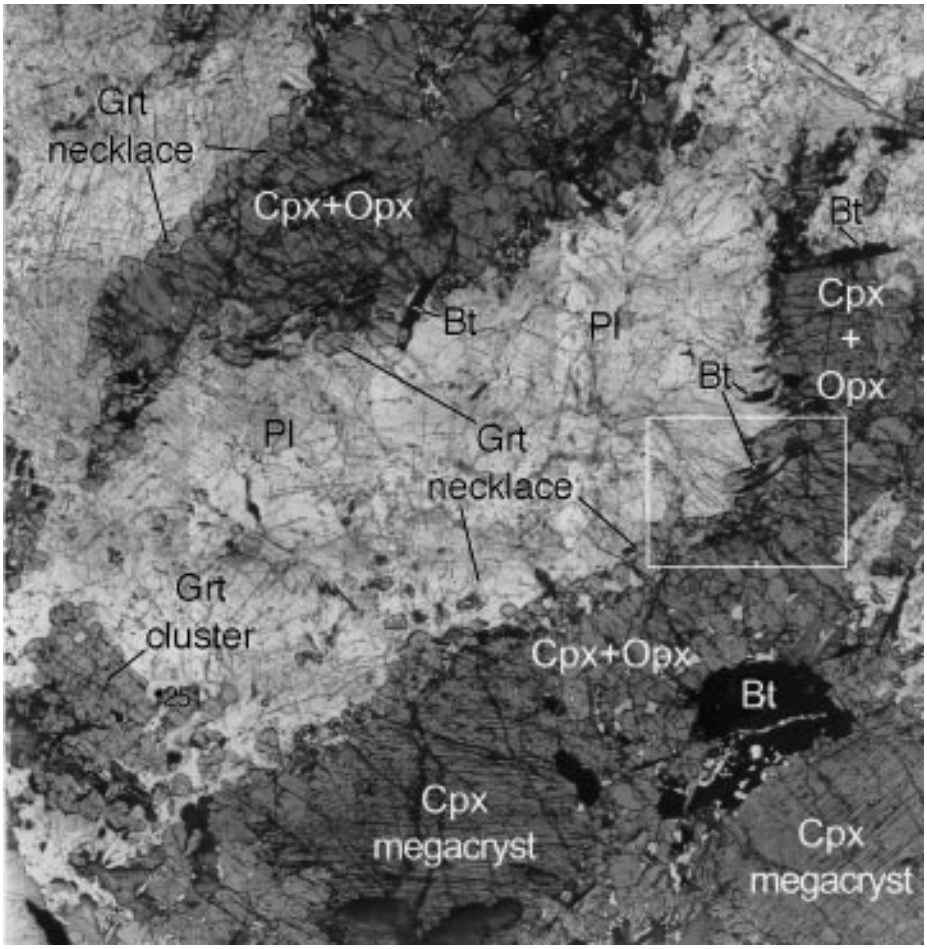


**Fig. 4.** Photomicrograph of sample ET-10. Clinopyroxene megacrysts are seen at lower right and lower center surrounded by metamorphic pyroxene. Cluster of garnet is seen in lower left and garnet necklaces are at the margin of metamorphic pyroxene and matrix plagioclase. Dark patches and blades are biotite. Box shows location of Fig. 6a. Width of field is 22 mm. Number indicates location of analysis in Table 1.

zoning in grossular is also observed, with core-to-rim variations on the order of 0·01 mol % (e.g. 0·19 in the core to 0·18 on the rim).

Plagioclase in this sample is unzoned, and there is no detectable compositional variation in the vicinity of garnet necklaces. However, regions of higher An content are observed locally (Fig. 5c).

A second detailed area of sample ET-10 illustrates zoning in metamorphic orthopyroxene plus the effect of the proximity of biotite on garnet zoning (Fig. 6). In garnet, Fe/(Fe+Mg) is only zoned where garnet and biotite touch (Fig. 6b) whereas in clinopyroxene, Fe/(Fe+Mg), Al and Ca are zoned symmetrically (Fig. 6d–f) from the core (bottom right) towards the rim. Significantly, the orthopyroxene inclusion within clinopyroxene is also zoned in Al and Fe/(Fe+Mg) in a fashion that mimics the Al and Fe/(Fe+Mg) zoning in the host clinopyroxene. It appears that as the orthopyroxene was being included in the clinopyroxene, partitioning equilibrium between the two phases was maintained. This zoning also suggests that diffusive processes have not substantially altered the Fe/(Fe+Mg) or Al zoning in either clinopyroxene or orthopyroxene. Plagioclase in this area is again unzoned, but patches of more calcic feldspar are observed near the reaction zone (Fig. 6c).

The texture in Fig. 6 also permits evaluation of the relative amount of zoning in clinopyroxene from garnet-absent reactions vs garnet-present reactions. In the garnet-absent sample (AS-31; Figs 3 and 4), orthopyroxene is typically found on the margin between metamorphic clinopyroxene and plagioclase. In contrast, in sample ET-10, orthopyroxene is found as inclusions within clinopyroxene, consistent with the garnet-producing reaction opx + pl = grt + cpx + qtz (see below). The clinopyroxene rim probably grew along with garnet as

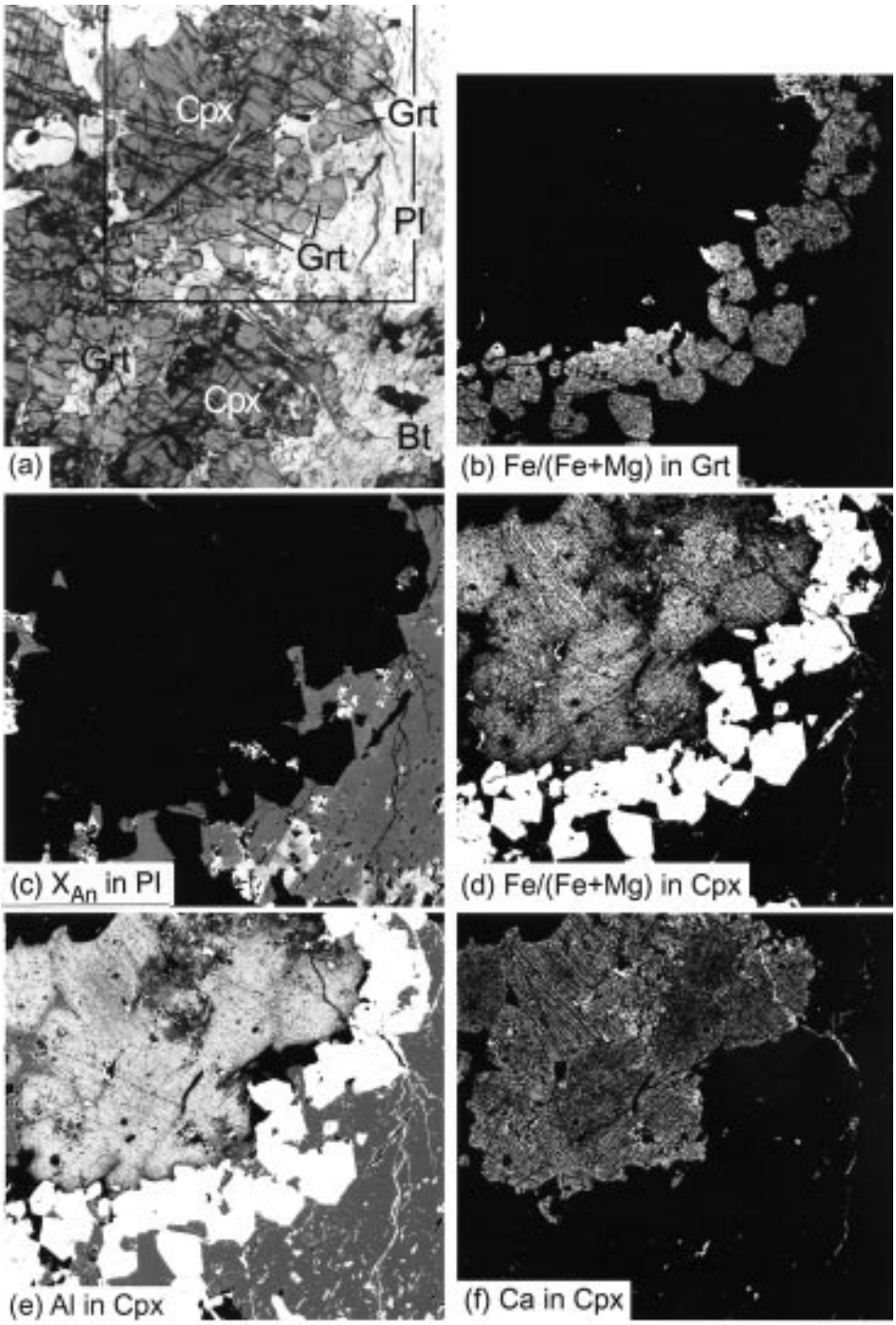


**Fig. 5.** Detail of garnet necklace–clinopyroxene reaction zone from sample ET-10. (a) Photomicrograph. Box shows location of X-ray maps (b–f). (b) Fe/(Fe+Mg) in garnet. (c) $X_{An}$ in plagioclase. (d) Fe/(Fe+Mg) in clinopyroxene. (e) Al in clinopyroxene. (f) Ca in clinopyroxene. [Note the increase in Fe/(Fe+Mg) seen in some garnet crystals towards the clinopyroxene interface, interpreted as the result of garnet growth by reaction (4).] Clinopyroxene shows core-to-rim increase in Ca (f) and decrease in Al (e) and Fe/(Fe+Mg) (d) that is symmetrically disposed around grain boundaries. [Note that the lowest Fe/(Fe+Mg) in clinopyroxene is seen along the contact with garnet.] Plagioclase is unzoned, but contains patches of higher An content in the vicinity of the reaction zone (c). Width of field in (a) is 9 mm.

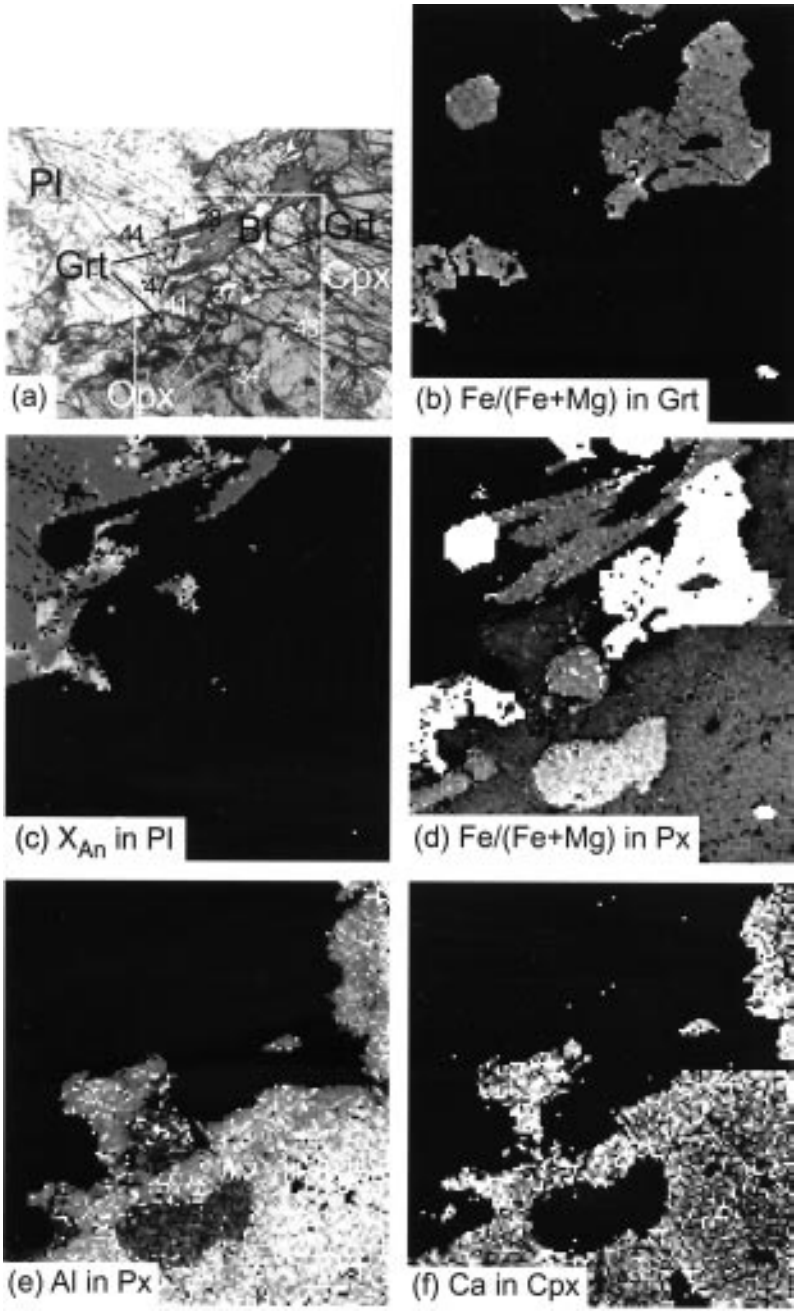


**Fig. 6.** Detail of garnet necklace–clinopyroxene–orthopyroxene–biotite reaction zone from sample ET-10. (a) Photomicrograph. Box shows location of X-ray maps (b–f). (b) Fe/(Fe+Mg) in garnet. [Note the increase in Fe/(Fe+Mg) towards contacts with biotite, interpreted as the result of diffusion driven by Fe–Mg exchange with biotite during cooling.] (c) $X_{An}$ in plagioclase. [Note the patches of high-An plagioclase in the reaction zone.] (d) Fe/(Fe+Mg) in clinopyroxene and orthopyroxene. (e) Al in clinopyroxene and orthopyroxene. [Note the decrease in Fe/(Fe+Mg) and Al towards the reaction zone (rim) in both pyroxenes.] (f) Ca in clinopyroxene. [Note the increase towards the rim.] Width of field in (a) is 4·8 mm. Numbers indicate location of analyses in Table 1.

orthopyroxene was consumed. Therefore, the zoning on the rim of the clinopyroxene external to the orthopyroxene inclusion may be attributed to the garnet-producing reaction.

Garnet in garnet clusters (Fig. 4) is only weakly zoned in Fe/(Fe+Mg) and this zoning is restricted to garnet in contact with biotite.

### SAR-1

Sample SAR-1 has the highest Fe/(Fe+Mg) of the suite and contains a superb example of garnet necklace texture (Fig. 7) between pyroxene and plagioclase. Orthopyroxene megacrysts have reacted during metamorphism to form interior crystals of clinopyroxene, plus clinopyroxene on the margins adjacent to plagioclase. The distribution of clinopyroxene can be seen as dark gray patches in Fig. 7b, which is an X-ray composition map showing the distribution of Fe/(Fe+Mg) in the sample. As in samples AS-31 and ET-10, clinopyroxene is zoned from core to rim with decreasing Al, Ca, and Fe/(Fe+Mg) (Fig. 8c and d) and only minor variation in Na (<0·01 cations/6 oxygens).

Plagioclase is zoned from $An_{46}$ in the core to $An_{40}$ on the margin (Figs 7c and 8e). Moreover, the reaction zone containing garnet is embedded in an aggregate of secondary plagioclase of $An_{40–45}$ composition. This texture suggests that the production of garnet was accompanied by recrystallization of plagioclase with more albitic compositions.

A detail of the reaction zone (Fig. 8) shows what is interpreted to be an example of grain boundary migration following garnet production. In most places in the thin section, garnet is surrounded by a zone of millimeter-sized grains of $An_{40–45}$ plagioclase. However, locally, garnet is entirely enclosed in plagioclase that is optically continuous with primary igneous plagioclase. Inasmuch as garnet growth postdates the igneous event, this could only result if the early plagioclase incorporated the later plagioclase by the process of grain boundary migration.

The detailed zoning maps for sample SAR-1 (Fig. 8) reveal that Fe/(Fe+Mg) in garnet increases as the reaction zone is approached and is highest on garnet rims in the reaction zone (Fig. 8b) (although this is difficult to detect in the gray-scale image). Fe/(Fe+Mg) and Al in pyroxene (Figs. 8c and d) decrease concentrically from core to rim in clinopyroxene and are irregular in orthopyroxene. The smooth zoning of plagioclase in the reaction zone is well displayed in Fig. 8e.

### Summary of reaction history as deduced from textures and mineral zoning

The following sequence of events is documented in these samples:

(1) Igneous mineralogy consisted of orthopyroxene and clinopyroxene (augite, orthopyroxene and pigeonite) megacrysts and plagioclase.

(2) Metamorphism resulted in the reaction of igneous pyroxenes producing exsolution and recrystallization into metamorphic ortho- and clinopyroxene. Metamorphic clinopyroxene produced at this stage is zoned toward decreasing Al and Fe/(Fe+Mg) and an increase in Ca from core to rim; orthopyroxene produced at this stage is zoned similarly in Al, but not as strongly as clinopyroxene. In sample AS-31 this reaction occurred in the absence of garnet.

(3) Garnet formed in selected samples producing clusters and necklaces by the reaction orthopyroxene + plagioclase = garnet + clinopyroxene + quartz. It is suspected that the clusters formed before the necklaces, but direct evidence for this is lacking. Garnet produced at this stage locally shows an increase in Fe/(Fe+Mg). Clinopyroxene grown at this stage shows a decrease in Al and Fe/(Fe+Mg) and increase in Ca.

(4) Zoning towards increasing Fe/(Fe+Mg) was produced in garnet in contact with biotite, presumably by Fe–Mg exchange during cooling.

## MINERAL CHEMISTRY

Shown in Table 1 are analyses representative of the extremes in composition observed in samples AS-31, ET-10 and SAR-1. These samples were chosen for tabulation because they are considered representative of the reaction histories observed in the suite, and they span the observed range of bulk Fe/(Fe+Mg) (AS-31 lowest, ET-10 intermediate, SAR-1 highest). Figures 2–8 show the location of each analysis listed in the table. All analyses were performed on a JEOL 733 electron microprobe following analytical procedures described by Kohn *et al.* (1993). Pyroxene megacryst compositions were measured by averaging the results of 50–200 analyses collected along line scans using a 10-μm beam diameter.

Using ET-10 as an example, garnet clusters (point 251) have Fe/(Fe+Mg) slightly lower than the cores of garnets in necklaces (point 7) (0·733 vs 0·755, respectively) and garnet touching biotite has Fe/(Fe+Mg) of 0·825, resulting from Fe–Mg exchange with biotite on cooling. Metamorphic orthopyroxene is zoned, with core-to-rim variations of Fe/(Fe+Mg) ranging from 0·498 to 0·451 and Al ranging from 0·093 to 0·056 cations/6 oxygens (all Fe as $Fe^{2+}$). Clinopyroxene is similarly zoned, with core-to-rim variations of Fe/(Fe+Mg) ranging from 0·394 to 0·328 and Al ranging from 0·145 to 0·113 cations/6 oxygens. Clinopyroxene is also zoned slightly in Ca, with core values slightly lower (0·85 cations/6 oxygens) compared with rim values (0·91 cations/6

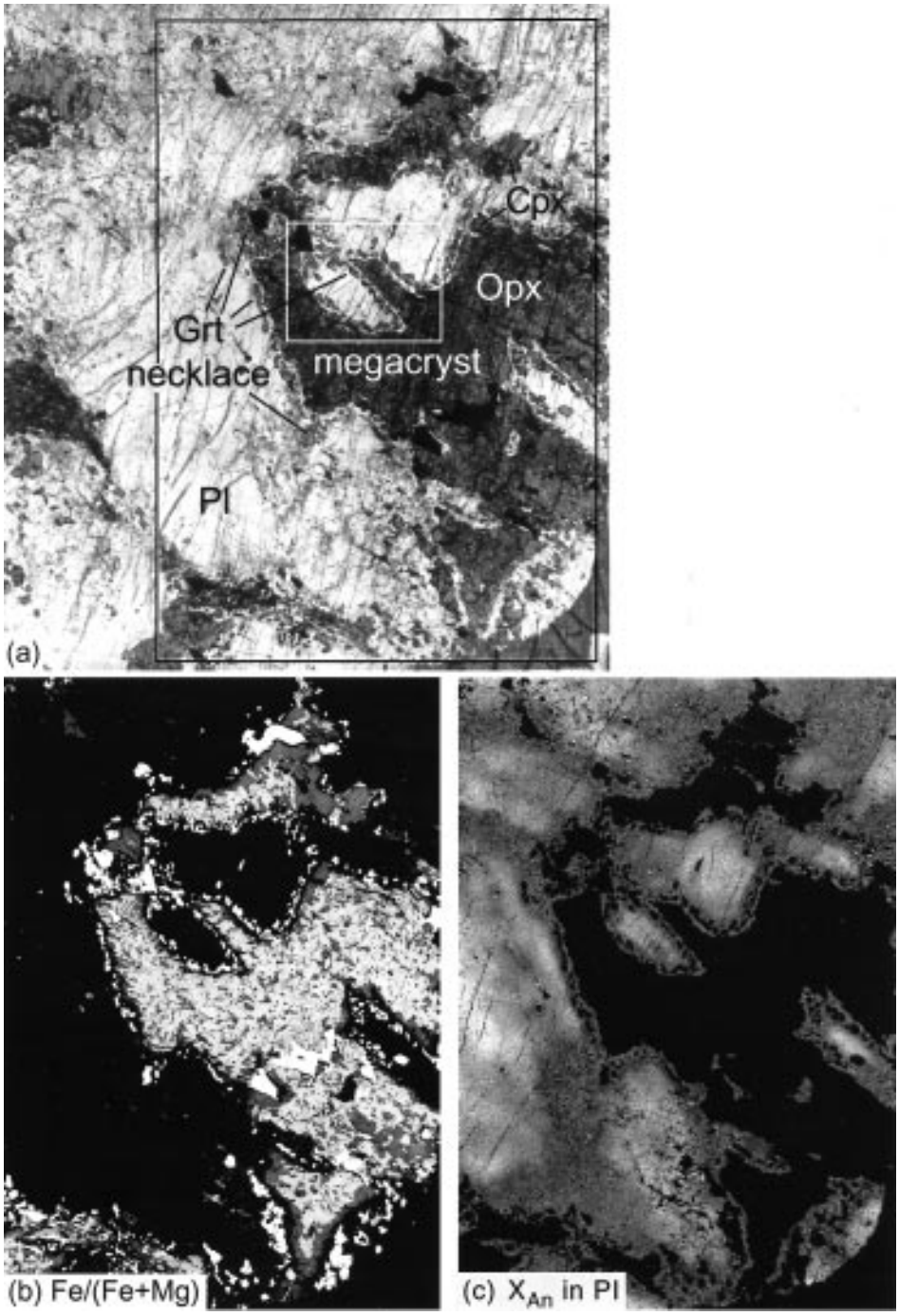


**Fig. 7.** Sample SAR-1. (a) Photomicrograph showing orthopyroxene megacryst (center of pyroxene cluster) surrounded by reaction zone of clinopyroxene + garnet + plagioclase + quartz. Width of field is 18 mm. Large box shows location of X-ray maps (b and c); small box shows location of Fig. 8. (b) Fe/(Fe + Mg) composition map showing distribution of oxides + garnet (white), orthopyroxene (light gray), clinopyroxene (dark gray) and feldspar + quartz (black). Clinopyroxene occurs both as patches within orthopyroxene megacryst and along the margins in the reaction zone. (c) Composition map showing zoning of $X_{An}$ in plagioclase from high values in the core ($X_{An} = 0{\cdot}47$) to lower values in the reaction zone ($X_{An} = 0{\cdot}40$).

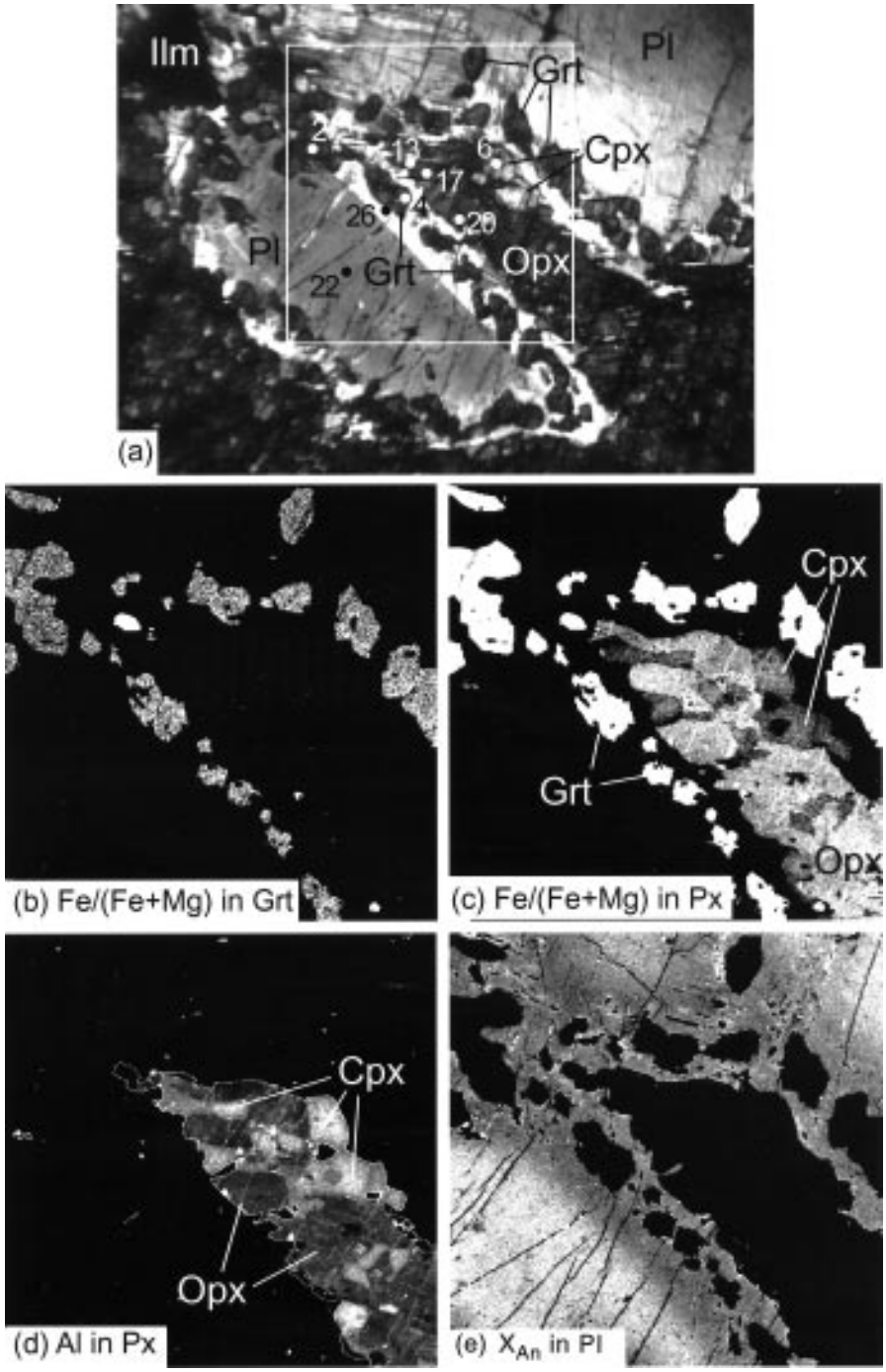


**Fig. 8.** Detail of reaction zone from sample SAR-1. (a) Photomicrograph in partially crossed polars. Some garnet is contained within optically continuous large plagioclase crystals whereas other garnet is in a polycrystalline reaction zone. Width of field is 4·7 mm. Box shows location of X-ray maps (b–e). (b) Fe/(Fe+Mg) distribution in garnet. Garnet at upper left has lower (darker gray) Fe/(Fe+Mg) than garnet in the reaction zone and the garnet in the reaction zone is zoned towards higher Fe/(Fe+Mg) on the rim. (c) Fe/(Fe+Mg) distribution in pyroxene. Clinopyroxene shows symmetrical decrease in Fe/(Fe+Mg) from core to rim whereas orthopyroxene shows patchy Fe/(Fe+Mg) zoning. (d) Distribution of Al in clinopyroxene (light gray) and orthopyroxene (darker gray). Al decreases in each pyroxene from core to rim. (e) Detail of plagioclase zoning in the reaction zone. $X_{An}$ decreases from $X_{An}=46$ in the core to $X_{An}=40$ towards the zone, then increases slightly to $X_{An}=43$ at the contact with pyroxene. Numbers indicate location of analyses in Table 1.

*Table 1: Selected chemical analyses of minerals from samples AS-31, ET-10 and SAR-1*

| | Garnet | | | | |
|---|---|---|---|---|---|
| | ET-10 | | | SAR-1 | |
| Point: | 1 | 7 | 251 | 2 | 4 |
| | rim | core | cluster | core | rim |
| $SiO_2$ | 37·26 | 37·98 | 38·55 | 37·46 | 37·07 |
| $Al_2O_3$ | 21·28 | 21·84 | 20·72 | 21·52 | 21·20 |
| MgO | 3·66 | 5·24 | 5·63 | 3·60 | 3·09 |
| FeO | 30·76 | 28·78 | 27·48 | 30·60 | 30·48 |
| MnO | 1·05 | 0·96 | 0·98 | 1·16 | 1·19 |
| CaO | 7·21 | 6·94 | 7·28 | 7·28 | 7·89 |
| Total | 101·22 | 101·75 | 100·65 | 101·63 | 100·92 |
| *Cations per 12 oxygens* | | | | | |
| Si | 2·940 | 2·946 | 3·009 | 2·944 | 2·942 |
| Al | 1·980 | 1·997 | 1·907 | 1·994 | 1·984 |
| Mg | 0·430 | 0·606 | 0·655 | 0·422 | 0·366 |
| $Fe^{2+}$ | 2·030 | 1·867 | 1·794 | 2·011 | 2·023 |
| Mn | 0·070 | 0·063 | 0·065 | 0·077 | 0·080 |
| Ca | 0·610 | 0·577 | 0·609 | 0·613 | 0·671 |
| Fe/(Fe+Mg) | 0·825 | 0·755 | 0·733 | 0·827 | 0·847 |
| Prp | 0·137 | 0·195 | 0·210 | 0·135 | 0·117 |
| Alm | 0·646 | 0·600 | 0·574 | 0·644 | 0·644 |
| Sps | 0·022 | 0·020 | 0·021 | 0·025 | 0·025 |
| Grs | 0·194 | 0·185 | 0·195 | 0·196 | 0·214 |

| | Biotite | | Amphibole | |
|---|---|---|---|---|
| | AS-31 | ET-10 | AS-31 | ET-10 |
| | 16 | 28 | 24 | 135 |
| $SiO_2$ | 37·01 | 36·13 | 42·00 | 45·05 |
| $Al_2O_3$ | 13·87 | 14·34 | 12·38 | 10·25 |
| $TiO_2$ | 3·60 | 5·19 | 1·35 | 1·11 |
| MgO | 13·13 | 12·04 | 10·14 | 12·59 |
| FeO | 17·17 | 19·10 | 16·01 | 15·01 |
| MnO | 0·06 | 0·02 | 0·11 | 0·10 |
| CaO | 0·07 | 0·00 | 11·44 | 12·05 |
| $Na_2O$ | 0·05 | 0·01 | 1·18 | 1·17 |
| $K_2O$ | 9·17 | 9·66 | 2·12 | 1·09 |
| F | 1·16 | 0·043 | 0·71 | 0·26 |
| Cl | 0·25 | 0·014 | 0·42 | 0·08 |
| Total | 94·14 | 96·48 | 96·72 | 98·41 |
| | *Cations per 22 oxygens* | | *Cations per 23 oxygens* | |
| Si | 5·658 | 5·462 | 6·386 | 6·640 |
| $Al^{iv}$ | 2·342 | 2·538 | 1·614 | 1·360 |
| $Al^{vi}$ | 0·157 | 0·017 | 0·605 | 0·422 |
| Ti | 0·414 | 0·590 | 0·154 | 0·123 |
| Mg | 2·991 | 2·712 | 2·298 | 2·766 |
| $Fe^{2+}$ | 2·195 | 2·415 | 2·036 | 1·850 |
| Mn | 0·008 | 0·002 | 0·014 | 0·012 |
| ΣOct | 5·766 | 5·737 | 5·107 | 5·173 |
| Ca | 0·001 | 0·000 | 1·864 | 1·903 |
| Na | 0·015 | 0·002 | 0·348 | 0·334 |
| K | 1·788 | 1·864 | 0·411 | 0·205 |
| $OH^1$ | 3·374 | 3·759 | 1·550 | 1·859 |
| F | 0·561 | 0·206 | 0·341 | 0·121 |
| Cl | 0·065 | 0·036 | 0·108 | 0·020 |
| Fe/(Fe+Mg) | 0·423 | 0·471 | 0·470 | 0·401 |

*Table 1: continued*

| | Orthopyroxene | | | | | | Clinopyroxene | | | | | |
|---|---|---|---|---|---|---|---|---|---|---|---|---|
| | AS-31 63 core | AS-31 62 rim | ET-10 34 core | ET-10 37 rim | SAR-1 17 core | SAR-1 20 rim | AS-31 51 core | AS-31 56 rim | ET-10 43 core | ET-10 265-41 rim | SAR-1 6 core | SAR-1 13 rim |
| $SiO_2$ | 50·06 | 49·61 | 49·76 | 51·03 | 48·45 | 47·61 | 49·48 | 50·94 | 48·70 | 51·15 | 49·15 | 49·19 |
| $Al_2O_3$ | 1·64 | 1·21 | 2·04 | 1·25 | 1·18 | 1·16 | 3·40 | 1·81 | 3·19 | 2·55 | 2·37 | 1·72 |
| $TiO_2$ | 0·03 | 0·00 | 0·03 | 0·03 | 0·07 | 0·07 | 0·46 | 0·25 | 0·38 | 0·25 | 0·28 | 0·17 |
| $Cr_2O_3$ | 0·00 | 0·00 | 0·00 | 0·00 | 0·06 | 0·09 | 0·07 | 0·03 | 0·00 | 0·00 | 0·03 | 0·00 |
| MgO | 17·86 | 18·05 | 17·22 | 19·48 | 13·04 | 14·36 | 11·93 | 12·64 | 11·81 | 12·36 | 9·92 | 10·54 |
| FeO | 29·53 | 29·66 | 30·47 | 28·54 | 35·64 | 35·39 | 11·36 | 10·63 | 13·70 | 10·74 | 16·82 | 14·44 |
| MnO | 0·53 | 0·55 | 0·43 | 0·31 | 0·44 | 0·47 | 0·22 | 0·19 | 0·18 | 0·13 | 0·21 | 0·15 |
| CaO | 1·98 | 1·84 | 0·51 | 0·44 | 0·65 | 0·44 | 21·03 | 22·87 | 20·66 | 22·59 | 21·14 | 22·66 |
| $Na_2O$ | 0·00 | 0·00 | 0·03 | 0·01 | 0·04 | 0·01 | 0·55 | 0·42 | 0·56 | 0·55 | 0·49 | 0·51 |
| Total | 101·66 | 100·96 | 100·49 | 101·11 | 99·58 | 99·61 | 99·20 | 99·78 | 99·17 | 100·30 | 100·41 | 100·11 |
| Si | 1·913 | 1·914 | 1·923 | 1·939 | 1·944 | 1·913 | 1·891 | 1·931 | 1·879 | 1·925 | 1·901 | 1·922 |
| $Al^{iv}$ | 0·074 | 0·055 | 0·077 | 0·056 | 0·056 | 0·055 | 0·109 | 0·069 | 0·121 | 0·075 | 0·099 | 0·078 |
| Al total | 0·074 | 0·055 | 0·093 | 0·056 | 0·056 | 0·055 | 0·151 | 0·081 | 0·145 | 0·113 | 0·108 | 0·078 |
| $Al^{vi}$ | 0·000 | 0·000 | 0·016 | 0·000 | 0·000 | 0·000 | 0·042 | 0·012 | 0·024 | 0·038 | 0·009 | 0·000 |
| Ti | 0·001 | 0·000 | 0·001 | 0·001 | 0·002 | 0·002 | 0·013 | 0·007 | 0·011 | 0·007 | 0·008 | 0·005 |
| $Cr^{3+}$ | 0·001 | 0·001 | 0·000 | 0·000 | 0·002 | 0·003 | 0·002 | 0·001 | 0·000 | 0·000 | 0·001 | 0·000 |
| Mg | 1·017 | 1·038 | 0·992 | 1·103 | 0·780 | 0·860 | 0·670 | 0·714 | 0·679 | 0·693 | 0·572 | 0·605 |
| $Fe^{2+}$ | 0·944 | 0·957 | 0·985 | 0·907 | 1·196 | 1·189 | 0·358 | 0·337 | 0·442 | 0·338 | 0·544 | 0·465 |
| Mn | 0·017 | 0·018 | 0·014 | 0·010 | 0·015 | 0·016 | 0·007 | 0·006 | 0·006 | 0·004 | 0·007 | 0·005 |
| Ca | 0·081 | 0·076 | 0·021 | 0·018 | 0·028 | 0·019 | 0·849 | 0·929 | 0·854 | 0·911 | 0·876 | 0·935 |
| Na | 0·000 | 0·000 | 0·002 | 0·001 | 0·003 | 0·001 | 0·040 | 0·031 | 0·042 | 0·040 | 0·037 | 0·038 |
| Fe/(Fe+Mg) | 0·481 | 0·480 | 0·498 | 0·451 | 0·605 | 0·580 | 0·348 | 0·321 | 0·394 | 0·328 | 0·487 | 0·435 |
| Wo | 0·040 | 0·037 | 0·011 | 0·009 | 0·014 | 0·009 | 0·452 | 0·469 | 0·432 | 0·469 | 0·440 | 0·466 |
| En | 0·498 | 0·501 | 0·496 | 0·544 | 0·389 | 0·416 | 0·357 | 0·361 | 0·344 | 0·357 | 0·287 | 0·302 |
| Fs | 0·462 | 0·462 | 0·493 | 0·447 | 0·597 | 0·575 | 0·191 | 0·170 | 0·224 | 0·174 | 0·273 | 0·232 |

| | Plagioclase | | | | | |
|---|---|---|---|---|---|---|
| | AS-31 27 core | AS-31 26 rim | ET-10 44 core | ET-10 47 patches | SAR-1 22 core | SAR-1 26 rim |
| An | 0·501 | 0·602 | 0·494 | 0·764 | 0·463 | 0·400 |
| Ab | 0·478 | 0·384 | 0·491 | 0·229 | 0·519 | 0·584 |
| Or | 0·021 | 0·014 | 0·015 | 0·007 | 0·018 | 0·016 |

[1] By difference.

oxygens). Similar relations are observed in sample SAR-1 and AS-31.

Garnet and pyroxene compositions from samples ET-10 and SAR-1 are shown in plots of $Al_2O_3$–FeO–MgO (AFM) and CaO–FeO–MgO (CFM) in Fig. 9. Tie lines have been drawn between pyroxene cores, which are not believed to have been in equilibrium with garnet, and between pyroxene rims and the composition of garnet believed to represent the last equilibration. It should be noted that analysis 1 from sample ET-10 is taken on the rim of garnet touching biotite, which is believed to have undergone Fe–Mg exchange during cooling, and is thus

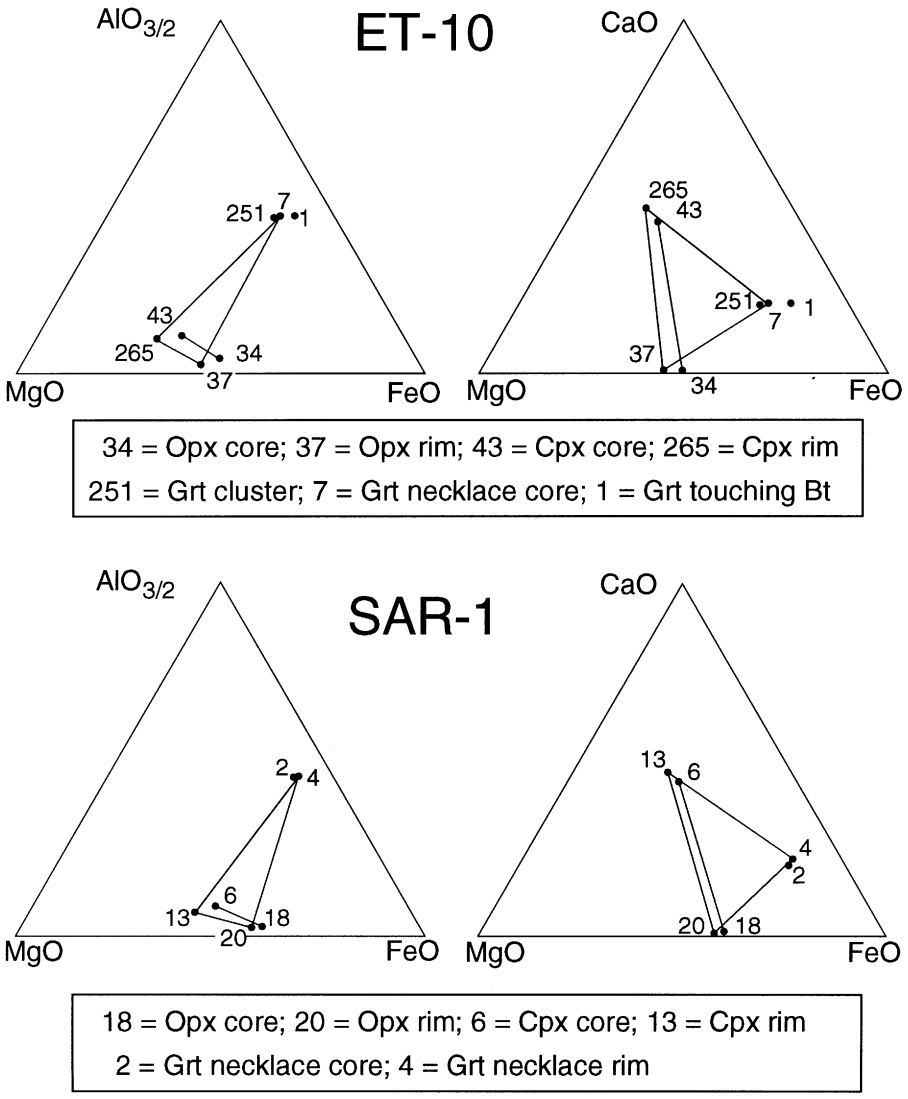


**Fig. 9.** AFM and CFM diagrams showing compositions of pyroxenes and garnets from samples ET-10 and SAR-1. Tie lines have been drawn between pyroxene rim and garnet rim compositions.

significantly higher in Fe/(Fe+Mg) than other garnet analyses.

Sample AS-31 is important, as discussed above, because it does not contain appreciable modal garnet. Significantly, clinopyroxene shows a decrease from core to rim in Al and Fe/(Fe+Mg) and an increase in Ca, as was also observed on the X-ray maps. However, comparison of the core-to-rim variations of sample AS-31 with those seen in ET-10 and SAR-1 reveals that the latter two samples have larger variations in Al and Fe/(Fe+Mg) and similar variation in Ca. This is interpreted to mean that some of the core-to-rim variation in Al and Fe/(Fe+Mg) is the result of garnet-absent reactions and some results from reactions in which garnet is present. This point will be returned to below.

## REACTION MODELING

In rocks containing zoned minerals, reaction modeling is a prerequisite to application of phase equilibria or thermobarometry because each requires an assessment of whether phases are in mutual equilibrium. There are three significant reactions to evaluate in the metaanorthosites studied here: (1) the reaction that produced the metamorphic clino- and orthopyroxene; (2) the

reaction that produced the garnet clots and necklaces; (3) the reaction that produced biotite.

## Production of metamorphic ortho- and clinopyroxene

Sample AS-31 contains an igneous pigeonite megacryst rimmed by metamorphic ortho- and clinopyroxene (+biotite+hornblende+ilmenite). Inasmuch as the sample contains only a trace amount of garnet, the observed zoning must be accounted for by garnet-absent reactions. From Fig. 3 it can be seen that clinopyroxene is zoned systematically with decreasing Al and Fe/(Fe+Mg) towards the rim. Orthopyroxene also zones rimward with decreasing Al, but there is no measurable change in Fe/(Fe+Mg) from core to rim. Plagioclase is zoned with increasing $X_{An}$ from the core towards the metamorphic pyroxene.

The reaction inferred for the production of metamorphic pyroxene involves the breakdown of the early ortho- and clinopyroxene megacrysts:

$$\text{Opx or Cpx megacryst} + \text{Plagioclase} = \text{metamorphic Opx} + \text{Cpx}. \quad (1)$$

To constrain the evolution of these samples, *P–T–X* contour diagrams for the assemblage clinopyroxene+orthopyroxene+plagioclase+quartz have been constructed using the Gibbs method (Spear *et al.*, 1982; Spear, 1989), and the results are shown in Fig. 10. Isopleths of Al in ortho- and clinopyroxene have negative slopes with Al contents increasing to higher temperature and pressure. Contours of Fe/(Fe+Mg) have nearly vertical slopes; in clinopyroxene, Fe/(Fe+Mg) decreases with decreasing temperature whereas in orthopyroxene, the ratio increases with decreasing temperature. Contours of $X_{An}$ in plagioclase (not shown) have nearly vertical slopes with $X_{An}$ increasing with decreasing $T$. A *P–T* vector has been drawn on the diagrams that accounts for the observed Al zoning in both pyroxenes, the Fe/(Fe+Mg) zoning in clinopyroxene, and the zoning in plagioclase. As noted above, Fe/(Fe+Mg) in orthopyroxene does not change measurably from core to rim, which is consistent with the wide spacing of these contours. Also noted above, no systematic zoning of Na was observed in clinopyroxene from sample AS-31, and the *P–T* vector has been drawn parallel to the Na contour consistent with this observation. It should be noted, however, that the *P–T* vector is rather sensitive to errors in Na but considerably less so to errors in Al and Fe/Mg determinations. To obtain quantitatively the observed amount of zoning, cooling of ~100°C is required.

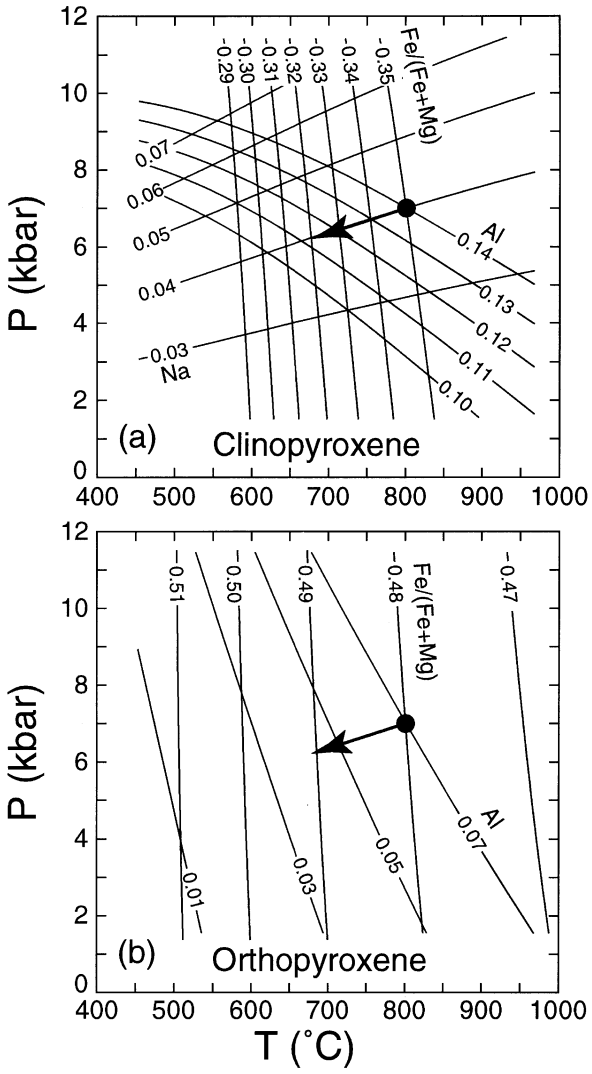


**Fig. 10.** Pressure–temperature diagrams showing contours for Fe/(Fe+Mg), Al and Na in clinopyroxene (a) and Fe/(Fe+Mg) and Al in orthopyroxene (b) for the assemblage clinopyroxene+orthopyroxene+plagioclase+quartz. Arrow depicts a *P–T* path that is consistent with the observed zoning in pyroxene.

## Production of garnet

Garnet-producing reactions in similar rocks from the Adirondacks have been described by De Waard (1965) and McLelland & Whitney (1977), who, respectively, proposed the reactions

$$6\ \text{Orthopyroxene} + 2\ \text{Anorthite} = \text{Clinopyroxene} + \text{Garnet} + 2\ \text{Quartz} \quad (2)$$

and

$$(6-\alpha)\ \text{Orthopyroxene} + \alpha\ \text{Fe-Oxide} + (\alpha-2)\ \text{Quartz} = \text{Garnet} + \text{Clinopyroxene} \quad (3)$$

where $\alpha$ is a coefficient that depends on the distribution of Fe and Mg among phases. Similar reactions from mafic granulites from Enderby Land, Antarctica, have been described by Ellis & Green (1985). Depending on the amount of Fe and Mg present, quartz may be a product or a reactant in reaction (3). As discussed by McLelland & Whitney (1977), the key distinction between these two reactions is the presence of Fe-oxide in the latter, which is required for Fe mass balance, and is supported by the textural evidence of garnet necklaces surrounding oxides.

The results of Gibbs method modeling of the assemblage garnet + plagioclase + orthopyroxene + clinopyroxene + quartz are shown in Fig. 11 [see also Ellis & Green (1985), for an analysis of this assemblage using equilibrium constants]. That these diagrams be useful for the interpretation of the reaction history, several important points about the mineral zoning should be reiterated:

(1) Garnet Fe/(Fe + Mg) increases slightly from clusters to necklaces (e.g. ET-10) or from core to rim (e.g. ET-10, SAR-1).

(2) Grossular is very nearly constant in garnet, but locally decreases by 0·01 mole fraction from core to rim.

(3) Fe/(Fe + Mg) in both clino- and orthopyroxene decreases from core to rim but at least some of this zoning is produced in a garnet-absent assemblage.

(4) In clinopyroxene, Al decreases systematically from core to rim.

(5) In orthopyroxene, Al decreases from core to rim in some samples (e.g. ET-10) but is variable in others (e.g. SAR-1).

(6) Zoning in plagioclase is equivocal in some samples and systematic in others. In ET-10, most plagioclase is $An_{50}$ and there are patches of $An_{\sim 75}$ located near reaction zones. In SAR-1, most plagioclase is $An_{46}$ and zoning is systematic to $An_{40}$ in the reaction zones and back to $An_{43}$ at the contact with pyroxene.

A *P–T* vector with a slope of 6 bars/°C has been drawn in on the contour diagrams in Fig. 11; this vector appears to satisfy all of the above zoning constraints. A crucial observation is Fe/(Fe + Mg) zoning in garnet, which operates in the opposite direction to that in pyroxene. A *P–T* path that involves cooling and decreasing pressure crosses the Fe/(Fe + Mg) isopleths in a manner to produce this type of zoning (Fig. 11a). Grossular is relatively unzoned, and the broadly spaced contours (Fig. 11b) are consistent with this. This path is also consistent with Al zoning in pyroxene and plagioclase zoning. Figure 11c shows isopleths of garnet abundance, which also place a broad constraint on the path. Inasmuch as the reaction produces garnet, the cooling path cannot have a slope greater than the 0·0 garnet molar abundance isopleth.

The stoichiometry of the balanced reaction depends on the actual *P–T* path followed. For the *P–T* path shown in Fig. 11, the reaction stoichiometry has been calculated using the Gibbs method and the results are shown in Fig. 12. Also shown is a schematic AFM diagram depicting the change in garnet and pyroxene compositions along this path. From Fig. 12a it can be seen that production of ~5 vol % garnet requires ~60°C decrease in temperature (along a path with a slope of 6 bars/°C); the balanced reaction for this change in $T$ and $P$ is

$$4\ \mathrm{Opx} + 4\ \mathrm{Pl} = 5\ \mathrm{Grt} + 1\ \mathrm{Cpx} + 1\ \mathrm{Qtz}. \qquad (4)$$

Based on this stoichiometry, it can be inferred that a small amount of clinopyroxene is produced along with garnet.

### Production of biotite

Biotite is present in a number of samples up to a few modal per cent. Biotite has been observed as inclusions in metamorphic pyroxenes and garnet, so it is inferred that biotite formed at some time before cessation of the formation of the metamorphic pyroxenes.

The inferred reaction producing biotite involves breakdown of orthopyroxene plus K-feldspar component of plagioclase:

$$\mathrm{orthopyroxene} + \mathrm{K\text{-}feldspar} + \mathrm{H_2O} = \mathrm{biotite} + \mathrm{quartz}. \qquad (5)$$

This reaction is continuous in Fe and Mg with a positive $dP/dT$. The magnesian end-member reaction falls close to 1000°C at 6 kbar and $a(H_2O) = 1$ (e.g. Vielzeuf & Clemens, 1992) and the Fe end-member occurs at lower $T$. Presumably, $a(H_2O) \ll 1$ when biotite grew. Because of the small partitioning of Fe and Mg between biotite and orthopyroxene, the reaction spans a relatively narrow temperature interval from the Mg to the Fe end-members. Production of biotite occurs with decreasing temperature and, for the growth of 1–5 modal % as seen in the present suite of samples, a decrease in temperature of only 5–10°C is required. Biotite is inferred, therefore, to have grown during cooling as a result of the introduction of $H_2O$, F and Cl. This reaction places no special constraints on the *P–T* path.

## ESTIMATES OF *P–T* CONDITIONS

Estimates of peak *P–T* conditions cannot be made from petrogenetic grids because of the absence of *P–T* sensitive univariant equilibria in these rocks. Estimates of peak conditions must therefore rely on application of geothermometry and geobarometry. Application of thermobarometry is hindered because of several factors:

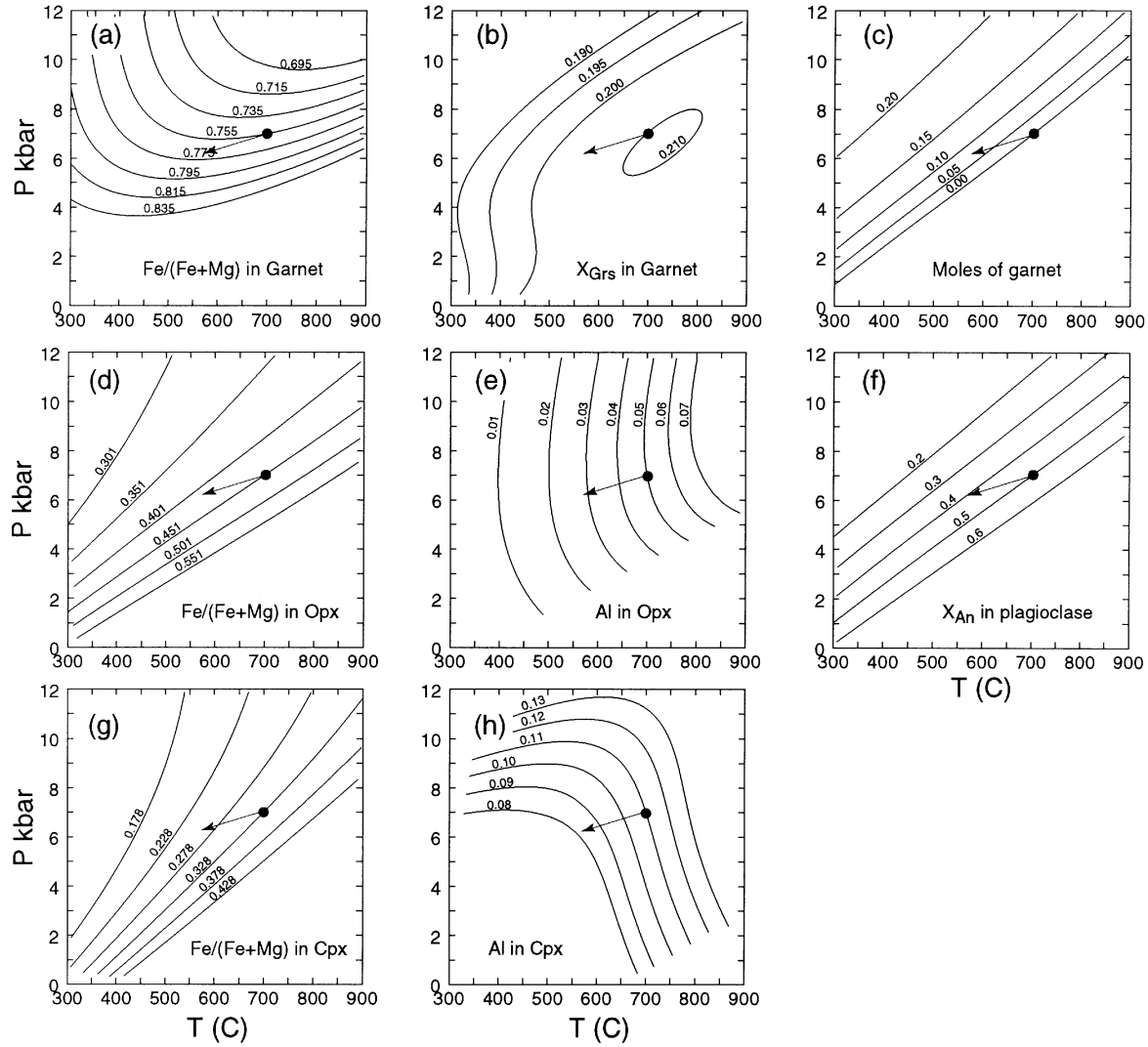


**Fig. 11.** Pressure–temperature diagrams showing contours for Fe/(Fe+Mg), $X_{Grs}$ and molar abundance in garnet (a), (b) and (c); Fe/(Fe+Mg) and Al in orthopyroxene and clinopyroxene (d), (e) and (g), (h), respectively; and $X_{An}$ in plagioclase (f) for the assemblage garnet+clinopyroxene+orthopyroxene+plagioclase+quartz. The arrow shows a *P*–*T* vector that is consistent with the observed zoning in all minerals.

(1) The minerals are chemically zoned, so it is impossible to infer with certainty the compositions that were at any time in mutual equilibrium.

(2) Zoning is the product of both growth processes and diffusion, and sorting out the relative contributions is difficult at best.

(3) Within a particular mineral system, there is no general agreement about the calibration of individual geothermobarometers, and especially the influence of minor components on the element partitioning.

(4) Several mineral systems are available for calculation, but there is no reliable cross-calibration between different systems.

The approach that is adopted here is to attempt to utilize the reaction history that has been worked out for the development of zoning in clino- and orthopyroxene, and the growth of garnet and biotite as a guide to determining which compositions to use for thermometry.

## Geothermometry

### *Two-pyroxene thermometry*

The earliest metamorphic reaction that has been identified is the growth of metamorphic clino- and orthopyroxene in the absence of garnet [reaction

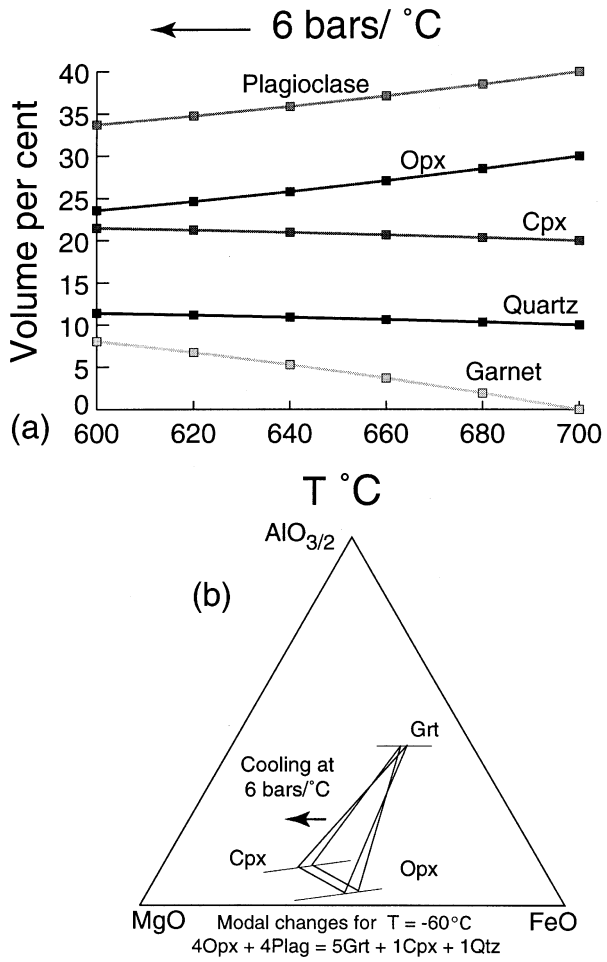


**Fig. 12.** (a) Plot of volume per cent of minerals vs temperature along a cooling path of 6 bars/°C. Garnet, quartz and clinopyroxene are produced at the expense of plagioclase and orthopyroxene. The measured modal amount of garnet (~5 vol %) requires a temperature decrease of ~60°C. (b) Schematic AFM diagram showing the shift in garnet and pyroxene compositions along a cooling path of 6 bars/°C.

(1)], igneous pyroxene megacryst + plagioclase = orthopyroxene + clinopyroxene. Compositions of pyroxene megacrysts are shown in Fig. 13 on the calculated pyroxene quadrilateral of Sack & Ghiorso (1994). All Fe was assumed to be ferrous for this plot inasmuch as the ferric iron normalization makes very little difference in the plotting position. Pyroxene megacrysts plot between the 1000 and 1100°C isotherms, indicative of the original igneous temperature of crystallization. A similar result was obtained from a study of pyroxene megacrysts from the Adirondack meta-anorthosite by Bohlen & Essene (1978).

As discussed above, the cores of the metamorphic clinopyroxenes have lower Ca contents than the rims and should represent compositions near the metamorphic peak, provided they have not been modified substantially by diffusion. The clinopyroxene rims are not interpreted to be in equilibrium with orthopyroxene rims, as a result of progress of reaction (4) and cannot be used for thermometry. A plot of the compositions of coexisting metamorphic ortho- and clinopyroxene cores and clinopyroxene rims is shown on the calculated pyroxene quadrilateral of Sack & Ghiorso (1994) (Fig. 14a,b). Metamorphic clinopyroxene cores plot between 800 and 850°C if all Fe is assumed to be $Fe^{2+}$ and between 650 and 700°C if ferric iron is calculated from stoichiometry.

The pyroxene quadrilateral is strictly valid only for pyroxenes in the CFMS system whereas natural pyroxenes invariably contain Al, Ti, $Fe^{3+}$, and Na. A method of projecting natural pyroxene compositions into the quadrilateral based on preservation of opx–cpx equilibrium relations is described in Appendix A, and the results of calculations on the coexisting clinopyroxene–orthopyroxene cores are shown in Fig. 14c. For this plot, the ferric iron normalized compositions (Fig. 14b) were used because only these analyses obey both charge balance and stoichiometry. The projection has the effect of shifting the compositions towards lower Wo content so that the projected compositions plot between 790 and 850°C.

The projection scheme described in Appendix A is the most accurate method known to the authors of plotting coexisting pyroxene pairs on the pyroxene quadrilateral. It should be pointed out that a nearly identical result would have been obtained had the thermodynamic pyroxene models of Sack & Ghiorso (1994) been formulated as a thermometer, inasmuch as both use similar thermodynamic constraints. Clearly, the ferric iron normalized plot (Fig. 14b) considerably underestimates the metamorphic temperature [compare Bohlen & Essene (1978)], but the thermodynamic projection (Fig. 14c) yields temperatures similar to the plot assuming all ferrous iron (Fig. 14a). This correspondence is fortuitous because the amount of 'correction' that results from the thermodynamic projection is a function of the amount of Al, $Fe^{3+}$, Ti, Cr and Na; that is, a pyroxene with considerable Al but very little calculated $Fe^{3+}$ would be corrected to somewhat higher temperature than that inferred from the all ferrous iron plot.

### *Garnet–clinopyroxene and garnet–orthopyroxene*

There is always ambiguity as to which compositions to choose for thermometry when minerals are zoned, and only in the context of a reaction model can meaningful selections be made. The reaction models discussed above suggest that clinopyroxene cores were in equilibrium with orthopyroxene and not garnet and should not be used with garnet for thermometry. The garnet-producing reaction produces clinopyroxene and consumes orthopyroxene, so garnet rims + clinopyroxene rims may be

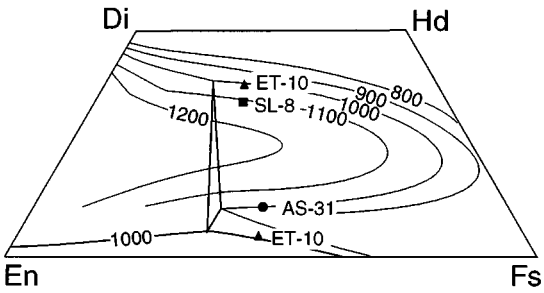


**Fig. 13.** Plots of the pyroxene quadrilateral showing the integrated compositions of pyroxene megacrysts from three samples (AS-31, ET-10, SL-8). The simple normalization scheme (see Appendix A) was used for these plots, so the temperatures of metamorphic pyroxenes are believed to be underestimated in these diagrams by 20–70°C.

inferred to represent equilibrated compositions. Whether garnet rims + orthopyroxene rims represent equilibrated compositions depends on the extent to which diffusion modifies orthopyroxene rim to maintain equilibrium with garnet as the orthopyroxene is consumed. In the absence of diffusion, the orthopyroxene rims would be relics of pre-garnet growth with clinopyroxene. Figures 10 and 11 may be used to evaluate the effect of orthopyroxene consumption on garnet–orthopyroxene thermometry. From Fig. 10b it is deduced that orthopyroxene will increase Fe/(Fe + Mg) by 0·01 as it reacts with clinopyroxene before garnet nucleates. From Fig. 11d, it is deduced that orthopyroxene rims will attempt to decrease in Fe/(Fe + Mg) by ~0·04 as garnet grows. The systematic decrease in Fe/(Fe + Mg) in orthopyroxene from core to rim seen in Fig. 6d argues strongly that orthopyroxene rims have maintained local equilibrium with clinopyroxene and garnet as garnet grows. Therefore, garnet–

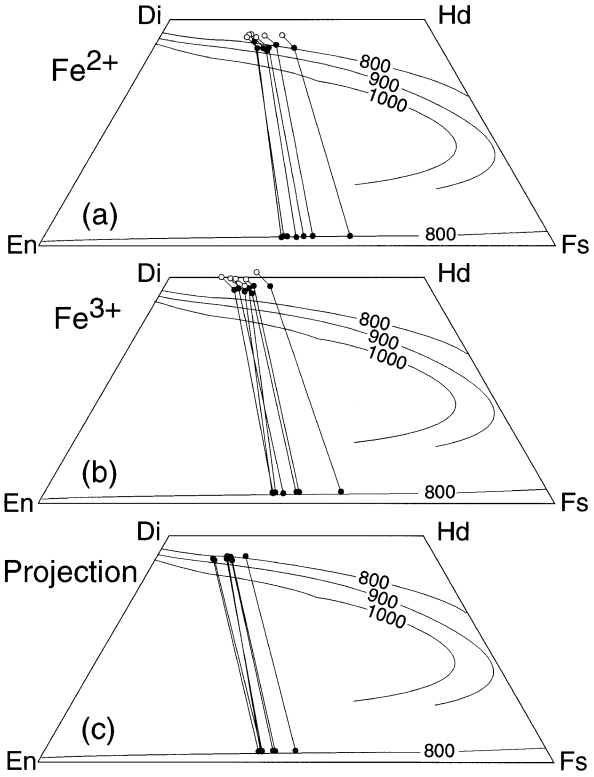


**Fig. 14.** Plots of the pyroxene quadrilateral showing the compositions of coexisting metamorphic orthopyroxene + clinopyroxene from all samples. Filled symbols are core compositions, open symbols rims (cpx only). (a) Simple normalization assuming all Fe is $Fe^{2+}$. (b) Simple normalization assuming $Fe^{3+}$ calculated from stoichiometric constraints. (c) Compositions of coexisting pyroxene cores plotted using the thermodynamic projection scheme described in Appendix A assuming $Fe^{3+}$ calculated from stoichiometric constraints.

orthopyroxene rims may be used for Fe–Mg exchange thermometry.

Results of Fe–Mg exchange thermometry on garnet + clinopyroxene rims and garnet + orthopyroxene rims are shown in Fig. 15. The calibration of Powell (1985) was used for garnet + clinopyroxene, but the Ellis & Green (1979) calibration gives very similar results. The calibration of Harley (1984*a*) was used for garnet + orthopyroxene rims; the calibration of Sen & Bhattacharya (1984) yields temperatures ~70°C higher. For comparison, results are shown assuming all Fe is $Fe^{2+}$ and with $Fe^{3+}$ estimated from stoichiometry. Average garnet + clinopyroxene and garnet + orthopyroxene rim temperatures are 735°C and 672°C assuming all Fe is $Fe^{2+}$, respectively, and 620°C and 634°C with $Fe^{3+}$ estimated from stoichiometry, respectively. For three reasons it is believed that the lower temperatures (assuming $Fe^{3+}$ from stoichiometry) correctly record the final equilibration of garnet + pyroxene. First, the thermometers were calibrated in the CFMAS system at relatively low $f(O_2)$, and presumably contain little ferric iron. Second, the similarity of grt + cpx and grt + opx temperatures (620 and 634°C) is consistent with all minerals equilibrating at the same time by reaction (4). Third, the $\Delta T$ required to produce pyroxene zoning was estimated to be 100°C (Fig. 10). Starting at the peak temperature of 800–850°C determined from coexisting pyroxene cores (Fig. 14c), this suggests that garnet nucleated around 700°C. The $\Delta T$ required to produce the observed modal garnet was 60°C (Fig. 12), suggesting garnet growth ended around 640°C, consistent with the lower garnet–pyroxene temperatures.

A further demonstration that the rim pyroxene compositions are equilibrated with garnet comes from sample AS-19E, which is the only sample that does not contain clinopyroxene. In this sample, orthopyroxene is unzoned, and both core and rim compositions give temperatures that are similar to garnet + orthopyroxene rim temperatures of the other samples (Fig. 15).

### *Garnet–biotite and garnet–hornblende*

Results of garnet–biotite thermometry using the calibration of Patiño-Douce *et al.* (1993) are shown in Fig. 16. This calibration is based on the experiments of Ferry & Spear (1978) and uses the garnet model of Berman (1990) to correct for the well-established Ca–Mg nonideality in garnet. It also accounts explicitly for the effects of Ti and $Al^6$ in biotite, which in these samples is typically >5 wt % $TiO_2$. Specifically, the effect of increasing $TiO_2$ is to decrease the calculated temperature and the effect of increasing $Al^6$ is the opposite. The magnitude of this correction for titaniferous biotites can be substantial. For example, garnet–biotite temperatures calculated for sample ET-10 using the data in Table 1 are 876°C without the Ti correction and 794°C with the correction.

Garnet–biotite temperatures range from 795 to 840°C, with the exception of two samples (SL-8, SR-18) with very low calculated temperatures. Biotite from both these samples contains large amounts of fluorine and modest amounts of chlorine, and there is a strong correlation between fluorine content and calculated temperature (Fig. 16b). The effect of F on Fe–Mg ratios in biotite has been discussed by a number of workers (e.g. see Munoz, 1984). The data shown here indicate there is a strong effect on the partitioning of Fe and Mg between biotite and garnet such that temperatures calculated from biotite with high F contents will be anomalously low.

Temperatures calculated from Fe–Mg partitioning between garnet and hornblende using the calibration of Graham & Powell (1984) range from 600 to 770°C (Fig. 16). The average of the garnet core–biotite temperatures for samples with low F is 817°C, which is almost 200 degrees higher than the temperatures inferred for garnet–pyroxene equilibration. Indeed, it is over 100 degrees higher than the inferred temperature for garnet nucleation. Moreover, temperatures calculated using garnet rim and matrix biotite range from 550 to 650°C, similar to garnet–pyroxene temperatures. However, garnet–biotite contacts show clear evidence for diffusional exchange of Fe and Mg (e.g. Fig. 6b) and ought to record closure temperatures that are lower than garnet–pyroxene temperatures. Garnet–hornblende temperatures, although not as extreme, are also higher than would be expected for well-equilibrated samples. The garnet–biotite and garnet–hornblende temperatures are, therefore, interpreted to be too high.

There are several possible reasons for the anomalously high garnet–biotite and garnet–hornblende temperatures: (1) disequilibrium; (2) inaccuracies in calibrations; (3) effects of reaction history and diffusive modification of compositions; (4) inaccurate characterization of biotite and hornblende compositions. The general systematics in element partitioning between phases rules out disequilibrium as a reasonable explanation. Calibration deficiencies may account for some of the difference. There is a small amount of Cl in every biotite measured. For example, the biotites in AS-31 and ET-10 contain 0·065 and 0·036 Cl per 22 oxygens, respectively. Based on the work of Kullerud (1995), Cl-bearing biotite–garnet temperatures should be corrected to lower temperatures in the amount of ~30°C for each $X_{Cl} = 0{\cdot}01$. The 'corrected' temperatures for the biotite–garnet thermometer for the present study should therefore be 30–60°C lower than those shown in Fig. 16.

The effects of diffusion during cooling are also potentially significant and must be considered. In a simple two-mineral system, Fe–Mg exchange during cooling will drive rim compositions of touching phases in opposite directions. This can clearly be seen to have occurred in

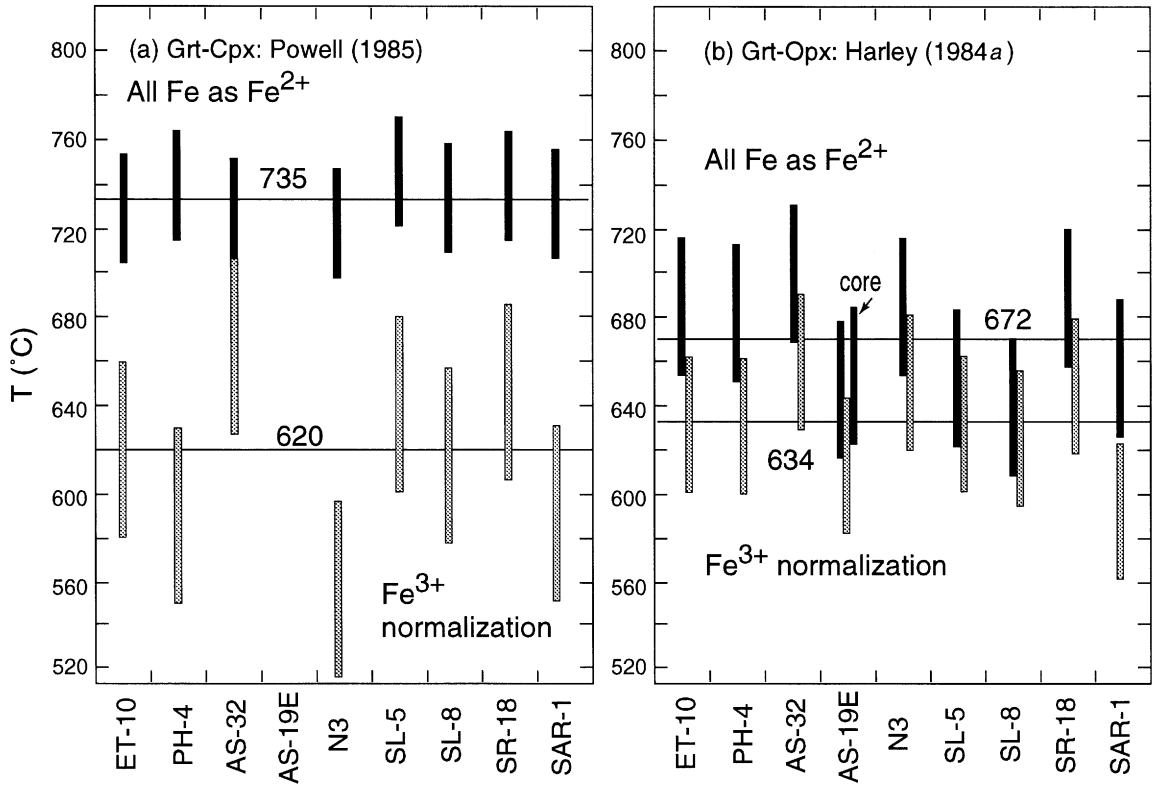


**Fig. 15.** Plot of calculated temperatures using Fe–Mg partitioning between garnet + pyroxene rims. Black rectangles: all Fe is $Fe^{2+}$; gray rectangles: $Fe^{3+}$ calculated from stoichiometric constraints. Length of rectangles reflects error associated with analytical uncertainty. Numbers and horizontal lines are average temperatures. (a) Garnet + clinopyroxene rim calculated using calibration of Powell (1985). (b) Garnet + orthopyroxene rim calculated using calibration of Harley (1984*a*). Rectangle labeled 'core' for sample AS-19E is temperature calculated using orthopyroxene core.

Fig. 6b at garnet–biotite interfaces. The composition of biotite cannot be considered as a two-mineral problem, however, because it commonly shares grain boundaries with garnet plus one or two pyroxenes (e.g. Fig. 6a). The relative Fe/Mg of the ferromagnesian phases is garnet>orthopyroxene>biotite>clinopyroxene, so garnet should always become more Fe rich and clinopyroxene should always become more Mg rich with Fe–Mg exchange during cooling. The changes expected in biotite depend on the relative diffusivities of Fe and Mg in the phases, which are $D_{FeMg}$ garnet$<D_{FeMg}$ clinopyroxene$\ll D_{FeMg}$ biotite. Therefore, garnet will close first to Fe–Mg exchange and the last equilibration will be between biotite and clinopyroxene. Inasmuch as biotite has a higher Fe/Mg than clinopyroxene, it will become more Fe rich with progressive exchange during cooling, resulting in a calculated garnet–biotite temperature that is higher than the temperature of equilibration. A change in biotite Fe/(Fe + Mg) of only 0·04 (e.g. 0·44–0·48) will raise the calculated temperature by 80°C. Biotite diffusion will continue even after clinopyroxene has closed, so biotite can homogenize resulting in apparently unzoned grains, as observed.

It is suspected, however, that inaccurate characterization of biotite and hornblende compositions is the major cause of the discrepancy. In particular, these minerals may have a considerable oxy component, consistent with the $H_2O$-poor environment of formation. Oxybiotites and oxyamphiboles have high ferric iron contents to maintain charge balance, and correction for ferric iron content will lower the Fe/(Fe + Mg) ratio of each, yielding lower garnet–biotite and garnet–hornblende temperatures. For example, a deficiency of ~1·0 H atom/24 oxygens in the biotite analysis from sample ET-10 (Table 1) would result in a $Fe^{3+}$/Fe total of ~0·4, which would lower the calculated temperature from 790°C to ~600°C. Verification of this suggestion requires direct determination of ferric iron content of biotite and hornblende.

## Geobarometry

Garnet + plagioclase geobarometers are useful in these samples because of the homogeneity of both phases.

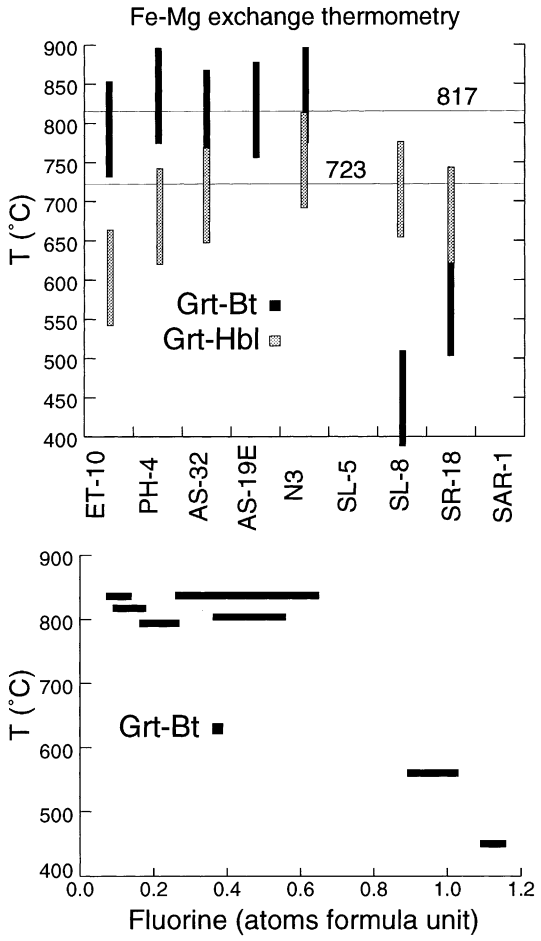


**Fig. 16.** (a) Plot of calculated temperatures using Fe–Mg partitioning between garnet + hornblende [gray bars; calibration of Graham & Powell (1984)] and garnet + biotite [black bars; calibration of Patiño-Douce *et al.* (1993)]. Average garnet + hornblende temperature, excluding sample ET-10, is 723°C. Average garnet–biotite temperature, excluding samples SL-8 and SR-18, is 817°C. Length of boxes reflects error associated with analytical uncertainty (±25°C). (b) Plot of calculated temperature vs F content for samples shown in (a). The effect of F is to lower the calculated temperature substantially.

Three geobarometers based on this equilibrium are suitable for this purpose:

garnet + plagioclase + clinopyroxene + quartz
garnet + plagioclase + orthopyroxene + quartz
garnet + plagioclase + hornblende + quartz.

Results of calculations with these three barometers are shown in Fig. 17. Pressures from the two garnet + plagioclase + pyroxene barometers give very consistent results of 6·5–7·5 kbar at 750°C, using the calibration of Eckert *et al.* (1991). Pressures obtained from the calibration of Moecher *et al.* (1988) are systematically 1·2–1·5 kbar higher. Garnet + plagioclase + hornblende barometry gives pressures that range from 7 to nearly 10 kbar and a much larger scatter. In general, these pressures are similar to those reported by Bohlen *et al.* (1985) of 7·5–8 kbar using a number of different barometers (see gray box).

## DISCUSSION

Figure 18 shows a summary of the *P–T* information gathered in this study combined with geochronologic constraints. Anorthosite crystallization is constrained by the compositions of early pyroxene megacrysts to have occurred at 1000–1100°C, consistent with the findings of Bohlen & Essene (1978). The pressure of crystallization of the anorthosite must have been low because the $Al_2O_3$ content of the igneous pyroxenes crystallized at 1000–1100°C is the same as the cores of the metamorphic clinopyroxenes crystallized starting at 900°C. Here the pressure is inferred to be 3–4 kbar based on extrapolation of the $Al_2O_3$ in clinopyroxene isochores from the metamorphic conditions down to the igneous conditions. Low-pressure crystallization of the anorthosite has been argued by Valley (1985), Valley *et al.* (1990), and Florence *et al.* (1995). Following anorthosite crystallization at ~1135 Ma (McLelland & Chiarenzelli, 1990), cooling to ambient conditions is shown in Fig. 18. In fact, there are few constraints on the thermal history between anorthosite crystallization and granulite facies metamorphism. Cooling is inferred because of the hiatus of igneous activity between 1135 and 1100 Ma (McLelland & Chiarenzelli, 1990).

The prograde metamorphic *P–T* path is shown as early heating accompanied by loading. The details of this path are not known, but it can be surmised that a clockwise *P–T* path is not tenable because of the nature of the crystallization history of garnet. Any *P–T* path that takes the rocks on a trajectory to pressures higher than the garnet 'isograd' molar isopleth in these bulk compositions (see Fig. 11c) would have produced garnet, which is not seen. Therefore, it is possible to rule out a clockwise prograde *P–T* path.

The maximum metamorphic temperature experienced by these rocks is ~800–850°C, based on two-pyroxene thermometry. The pressure of this early metamorphic history is constrained only by projection back along the *P–T* path from the pressure of final equilibration (~6·5–8 kbar). Pyroxene recrystallization proceeded with decreasing temperature and pressure along a cooling path of ~6 bars/°C. Pyroxene crystallization must have proceeded for 50–100°C to produce the observed zoning. At temperatures between 700 and 750°C, garnet began to crystallize. Based on the phase equilibria in Fig. 11, garnet growth began first in rocks with high Fe/(Fe + Mg) (e.g. SAR-1) and last in rocks with low Fe/(Fe + Mg) (e.g. PH-4). An approximate temperature of initiation of garnet crystallization can be inferred by backing up from

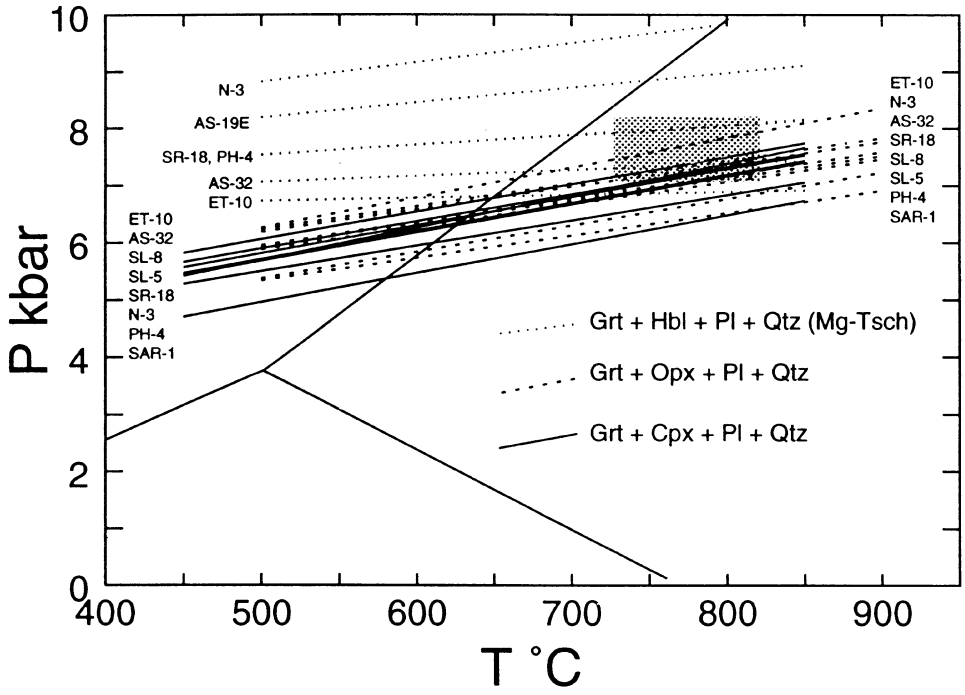


**Fig. 17.** *P–T* diagram showing the results of garnet + plagioclase barometry. Continuous lines are from garnet + plagioclase + clinopyroxene + quartz barometry, dashed lines are from garnet + plagioclase + orthopyroxene + quartz barometry [calibrations of Eckert *et al.* (1991)], dotted lines are from garnet + plagioclase + hornblende + quartz barometry [calibration of Kohn & Spear (1990)]. Gray box shows peak *P–T* conditions for central Adirondacks from Bohlen *et al.* (1985).

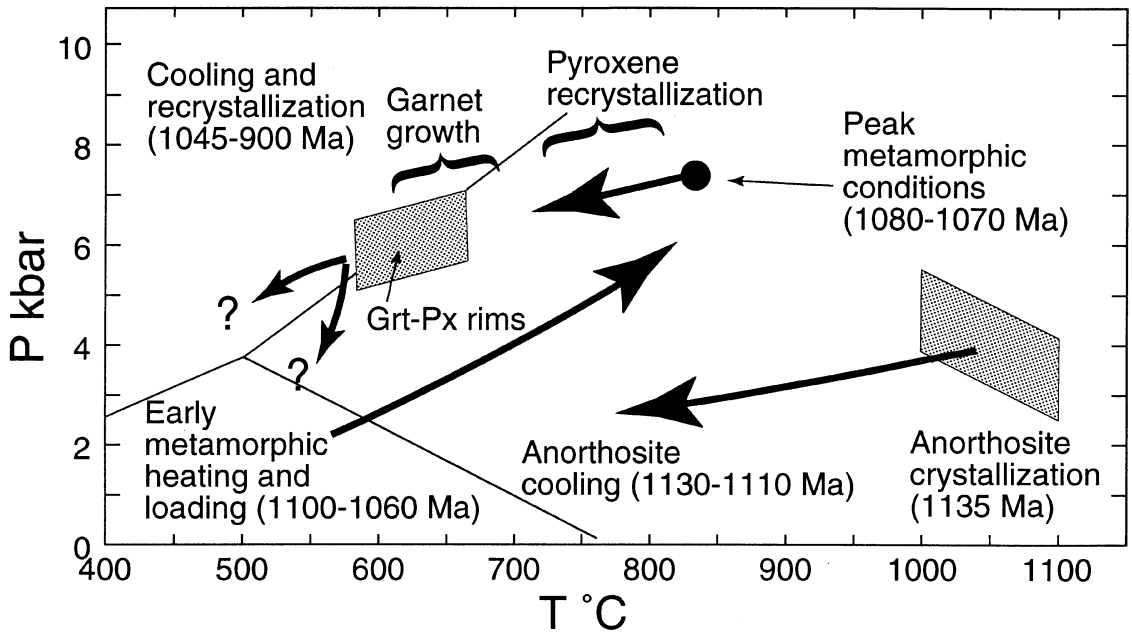


**Fig. 18.** *P–T* diagram summarizing the results of this and other studies on the *P–T* evolution of the Adirondack highlands with the geochronologic constraints summarized by McLelland & Chiarenzelli (1990).

the temperature of final garnet + pyroxene crystallization, which is ~630°C, to the point where initial garnet formed, which from the analysis given in Fig. 12 is approximately $\Delta T = 60$°C (i.e. 630 + 60 = 690°C for initial garnet nucleation). Finally, the $P$–$T$ path following the cessation of garnet growth is unconstrained by the data herein and two possibilities are indicated with question marks. Fluid inclusion data of Lamb *et al.* (1991) require the retrograde path to intersect relatively high-density $CO_2$ isochores, which could be achieved by either path.

This $P$–$T$ path shown in Fig. 18 is remarkably similar to that presented by Bohlen (1987) and qualitatively similar to that presented by Anovitz (1991). However, Anovitz (1991; see also Anovitz & Chase, 1990) presented a steeper initial cooling path for Grenville granulites, which he attributed to an earlier high-pressure history from a clockwise $P$–$T$ path. The absence of early formed garnet argues against early higher pressures in the central Adirondacks, and is consistent with a counterclockwise $P$–$T$ path following the intrusion of the Marcy Anorthosite.

The most reasonable interpretation of the counterclockwise $P$–$T$ path is that it represents an elevation of the geothermal gradient as the result of magma emplacement, followed by crustal thickening [compare Foose & McLelland (1995)]. Crustal thickening models (e.g. England & Thompson, 1984) typically show a temperature increase following nappe emplacement, but this is for the situation where crustal thickening results in a geotherm that is depressed (too cool at depth) relative to the steady-state geotherm. In the situation in which large-scale crustal heating precedes thickening, the local geotherm will be elevated relative to the steady-state geotherm, which typically goes through the kyanite field for shield rocks. Therefore, cooling will commence as soon as the heat source is removed. Cessation of large-scale magmatic activity in the Adirondacks occurred by 1050 Ma (McLelland & Chiarenzelli, 1990) and the timing of the metamorphic peak has been constrained to be ~1080–1070 Ma (J. McLelland, personal communication, 1996). The cause of crustal thickening is unknown, but pressures (6·5–8 kbar) imply that the crustal thickness was doubled at the metamorphic peak. The most likely interpretation is that the rocks at present exposed in the Adirondacks were the lower plate of a major crustal-scale thrust system during the ~1090–1050 Ma Ottawan phase of the Grenvillian Ottawan Cycle.

The metamorphic temperatures and pressures determined in this study are broadly consistent with those of other workers (e.g. Bohlen & Essene, 1979, 1980; Johnson & Essene, 1982; Johnson *et al.*, 1983; Bohlen *et al.*, 1985), although the peak two-pyroxene temperatures reported here are systematically higher than maximum temperatures reported by others [note, however, that Bohlen *et al.* (1985) did report a temperature as high as 820°C from near SAR-1: Fig. 1]. Indeed, two-pyroxene temperatures reported by Bohlen & Essene (1978) are on the order of 600°C, similar to 'unprojected', ferric-iron corrected temperatures obtained in this study (see Fig. 14b). The higher two-pyroxene temperatures reported here are the direct result of the improved projection scheme (Appendix A). Additionally, the scatter in the inferred garnet + pyroxene Fe–Mg exchange thermometry temperatures is smaller than reported in previous studies. In part, this decrease in scatter reflects the more limited range of metamorphic assemblages and reaction histories studied here. However, the results of this study also emphasize the need to analyze chemical zoning in great detail and to construct a reaction history before application of thermobarometry. For example, calculated garnet–pyroxene temperatures using pyroxene cores vs rims differ by 50–100°C and it was emphasized above that pyroxene cores were never in equilibrium with garnet. Moreover, previous studies reported limited zoning in garnet and pyroxene, but it was found to exist in all of the samples examined here. It is not surprising that this study uncovered zoning in most minerals. Before the routine usage of X-ray elemental mapping, zoning had been characterized by a few tens or hundreds of analyses. In contrast, a typical X-ray map is composed of many tens to hundreds of thousands of spot analyses, and several maps were typically collected on a single sample.

Geothermometry failed to reveal any systematic trends in metamorphic conditions across the central highlands, in contrast to the results of Bohlen *et al.* (1980, 1985) based on oxide and feldspar thermometry (Fig. 1). Within analytical uncertainty ($\pm 30$°C), temperatures from the Elizabethtown area are indistinguishable from those from the vicinity of Saranac Lake. However, it is most important to note that the systems studied by Bohlen & Essene (Fe–Ti oxides and two feldspars) are different from those examined here and may well be recording a different facet of the geological evolution. For example, it is very possible that the concentric isotherm pattern (e.g. Fig. 1) reflects some aspect of the thermal maximum before the appearance of garnet, which in this study was found to crystallize fairly late in the cooling history. Alternatively, the pattern may reflect some aspect of the cooling history of the Adirondacks.

Finally, it is important to emphasize that the interpretations of the compositional zoning are based on a reaction model and are apparently self-consistent. Most importantly, a reaction model is unique to an individual sample and a model that works on one assemblage will probably not work on a different assemblage. This point stresses the need to generate reaction models for each sample for which $P$–$T$ information is sought. It is simply not possible to generalize about whether core or rim (or some intermediate) composition is best representative of

the metamorphic peak. Only within the framework of a petrogenetic model can these inferences be made.

## ACKNOWLEDGEMENTS

The authors wish to thank Steve Bohlen and Jim McLelland for the contribution of samples used in this study and for very fruitful discussions about Adirondack geology. Reviews by M. Ayres, S. Harley, J. McLelland, and J. Valley helped improve the clarity of the presentation. This work was supported by NSF Grant EAR-9304804 to F.S.S., the Research Experiences for Undergraduates (REU) program at Rensselaer, and a Charles McMurrow undergraduate research award to J.M.M.

## REFERENCES

Anovitz, L. M., 1991. Al zoning in pyroxene and plagioclase: window on late prograde to early retrograde *P–T* paths in granulite terranes. *American Mineralogist* **76,** 1328–1343.

Anovitz, L. M. & Chase, C. G., 1990. Implications of post-thrusting extension and underplating for *P–T–t* paths in granulite terranes: a Grenville example. *Geology* **18,** 466–469.

Berman, R. G., 1988. Internally-consistent thermodynamic data for minerals in the system $Na_2O$–$K_2O$–CaO–MgO–FeO–$Fe_2O_3$–$Al_2O_3$–$SiO_2$–$TiO_2$–$H_2O$–$CO_2$. *Journal of Petrology* **29,** 445–522.

Berman, R. G., 1990. Mixing properties of Ca–Mg–Fe–Mn garnets. *American Mineralogist* **75,** 328–344.

Berman, R. G. & Brown, T. H., 1985. The heat capacity of minerals in the system $K_2O$–$Na_2O$–CaO–MgO–FeO–$Fe_2O_3$–$Al_2O_3$–$SiO_2$–$TiO_2$–$H_2O$–$CO_2$: representation, estimation, and high temperature extrapolation. *Contributions to Mineralogy and Petrology* **89,** 168–183.

Bohlen, S. R., 1987. Pressure–temperature–time paths and a tectonic model for the evolution of granulites. *Journal of Geology* **95,** 617–632.

Bohlen, S. R. & Essene, E. J., 1978. Igneous pyroxenes from metamorphosed anorthosite massifs. *Contributions to Mineralogy and Petrology* **65,** 433–442.

Bohlen, S. R. & Essene, E. J., 1979. A critical evaluation of two-pyroxene thermometry in Adirondack granulites. *Lithos* **12,** 335–345.

Bohlen, S. R. & Essene, E. J., 1980. Evaluation of coexisting garnet–biotite, garnet–clinopyroxene and other Fe–Mg exchange thermometers in Adirondack granulites. *Geological Society of America Bulletin* **91,** 685–719.

Bohlen, S. R., Essene, E. J. & Hoffman, K. S., 1980. Update on feldspar and oxide thermometry in the Adirondack Mountains, New York. *Geological Society of America Bulletin* **91,** 110–113.

Bohlen, S. R., Valley, J. W. & Essene, E. J., 1985. Metamorphism in the Adirondacks. I. Petrology, pressure and temperature. *Journal of Petrology* **26,** 971–992.

De Waard, D., 1965. The occurrence of garnet in the granulite-facies terrane of the Adirondack Highlands. *Journal of Petrology* **6,** 165–191.

Eckert, J. O. J., Newton, R. C. & Kleppa, O. J., 1991. The $\Delta H$ of reaction and recalibration of garnet–pyroxene–plagioclase–quartz geobarometers in the CMAS system by solution calorimetry. *American Mineralogist* **76,** 148–160.

Ellis, D. J. & Green, E. H., 1979. An experimental study of the effect of Ca upon garnet–clinopyroxene Fe–Mg exchange equilibria. *Contributions to Mineralogy and Petrology* **71,** 13–22.

Ellis, D. J. & Green, D. H., 1985. Garnet-forming reactions in mafic granulites from Enderby Land, Antarctica—implications for geothermometry and geobarometry. *Journal of Petrology* **26,** 633–662.

England, P. C. & Thompson, A. B., 1984. Pressure–temperature–time paths of regional metamorphism, Part I: Heat transfer during the evolution of regions of thickened continental crust. *Journal of Petrology* **25,** 894–928.

Ferry, J. M. & Spear, F. S., 1978. Experimental calibration of the partitioning of Fe and Mg between biotite and garnet. *Contributions to Mineralogy and Petrology* **66,** 113–117.

Florence, F. P., Darling, R. S. & Orrell, S. E., 1995. Moderate pressure metamorphism and anatexis due to anorthosite intrusion, western Adirondack Highlands, New York. *Contributions to Mineralogy and Petrology* **121,** 424–436.

Foose, M. P. & McLelland, J. M., 1995. Proterozoic low-Ti iron-oxide deposits in New York and New Jersey: relation to Fe-oxide (Cu–U–Au–rare earth element) deposits and tectonic implications. *Geology* **23,** 665–668.

Graham, C. M. & Powell, R., 1984. A garnet–hornblende geothermometer: calibration, testing, and application to the Pelona Schist, Southern California. *Journal of Metamorphic Geology* **2,** 13–21.

Harley, S. L., 1984*a*. An experimental study of partitioning of Fe and Mg between garnet and orthopyroxene. *Contributions to Mineralogy and Petrology* **86,** 359–373.

Harley, S. L., 1984*b*. The solubility of alumina in orthopyroxene coexisting with garnet in FeO–MgO–$Al_2O_3$–$SiO_2$ and CaO–FeO–MgO–$Al_2O_3$–$SiO_2$. *Journal of Petrology* **25,** 665–696.

Holland, T. J. B., 1989. Dependence of entropy on volume for silicate and oxide minerals: a review and a predictive mode. *American Mineralogist* **74,** 5–13.

Johnson, C. A. & Essene, E. J., 1982. The formation of garnet in olivine-bearing metagabbros from the Adirondacks. *Contributions to Mineralogy and Petrology* **81,** 240–251.

Johnson, C. A., Bohlen, S. R. & Essene, E. J., 1983. An evaluation of garnet–clinopyroxene geothermometry in granulites. *Contributions to Mineralogy and Petrology* **84,** 191–198.

Kohn, M. J. & Spear, F. S., 1990. Two new barometers for garnet amphibolites with applications to southeastern Vermont. *American Mineralogist* **75,** 89–96.

Kohn, M. J., Spear, F. S. & Dalziel, I. W. D., 1993. Metamorphic *P–T* paths from Cordillera Darwin, a core complex in Tierra del Fuego, Chile. *Journal of Petrology* **34,** 519–542.

Kullerud, K., 1995. Chlorine, titanium and barium-rich biotites: factors controlling composition and the implications for garnet–biotite geothermometry. *Contributions to Mineralogy and Petrology* **120,** 42–59.

Lamb, W. M., Brown, P. E. & Valley, J. W., 1991. Fluid inclusions in Adirondack granulites—implications for the retrograde *P–T* path. *Contributions to Mineralogy and Petrology* **107,** 472–483.

McLelland, J. & Chiarenzelli, J., 1990. Isotopic constraints on emplacement age of anorthositic rocks of the Marcy massif, Adirondack Mts., New York. *Journal of Geology* **98,** 19–41.

McLelland, J. M. & Whitney, P., 1977. Origin of garnet coronas in the anorthosite–charnockite suite of the Adirondacks. *Contributions to Mineralogy and Petrology* **60,** 161–181.

Moecher, D. P., Essene, E. J. & Anovitz, L. M., 1988. Calculation and application of clinopyroxene–garnet–plagioclase–quartz geobarometers. *Contributions to Mineralogy and Petrology* **100,** 92–106.

Munoz, J. L., 1984. F–OH and Cl–OH exchange in micas with applications to hydrothermal ore deposits. In: Bailey, S. W. (ed.) *Micas, Vol. 13*. Washington, DC: Mineralogical Society of America, pp. 469–494.

Patiño Douce, A. E., Johnston, A. D. & Rice, J. M., 1993. Octahedral excess mixing properties in biotite: a working model with applications

to geobarometry and geothermometry. *American Mineralogist* **78,** 113–131.

Powell, R., 1985. Regression diagnostics and robust regression in geothermometer/geobarometer calibration: the garnet–clinopyroxene geothermometer revisited. *Journal of Metamorphic Geology* **3,** 231–243.

Sack, R. O. & Ghiorso, M. S., 1994. Thermodynamics of multicomponent pyroxenes: II. Phase relations in the quadrilateral. *Contributions to Mineralogy and Petrology* **116,** 287–300.

Sen, S. K. & Bhattacharya, A., 1984. An orthopyroxene–garnet thermometer and its application to the Madras charnockites. *Contributions to Mineralogy and Petrology* **88,** 64–71.

Spear, F. S., 1988. Thermodynamic projection and extrapolation of high-variance mineral assemblages. *Contributions to Mineralogy and Petrology* **98,** 346–351.

Spear, F. S., 1989. Petrologic determination of metamorphic pressure–temperature–time paths. In: Spear, F. S. & Peacock, S. M. (eds) *Metamorphic Pressure–Temperature–Time Paths, Short Course in Geology*. Washington, DC: American Geophysical Union, pp. 1–55.

Spear, F. S., Ferry, J. M. & Rumble, D., 1982. Algebraic formulation of phase equilibria: the Gibbs method. In: Ferry, J. M. (ed.) *Characterization of Metamorphism through Mineral Equilibria, Vol. 10*. Washington, DC: Mineralogical Society of America, pp. 105–152.

Thompson, J. B., Jr, 1957. The graphical analysis of mineral assemblages in pelitic schists. *American Mineralogist* **42,** 842–858.

Valley, J. W., 1985. Polymetamorphism in the Adirondacks: wollastonite at the contacts of shallowly intruded anorthosite. In: Tobi, A. C. & Touret, J. L. R. (eds) *The Deep Proterozoic Crust in the North Atlantic Provinces*. Dordrecht: D. Reidel, pp. 217–237.

Valley, J., Bohlen, S. R., Essene, E. J. & Lamb, W., 1990. Metamorphism in the Adirondacks, II. The role of fluids. *Journal of Petrology* **31,** 555–596.

Vielzeuf, D. & Clemens, J. D., 1992. The fluid-absent melting of phlogopite + quartz: experiments and models. *American Mineralogist* **77,** 1206–1222.

## APPENDIX A: PROJECTION ONTO THE PYROXENE QUADRILATERAL

The pyroxene quadrilateral has been used extensively to infer temperatures of pyroxene crystallization from pyroxene chemistry, but there is no general consensus on the best way to account for 'non-quadrilateral' components in the plotting scheme. Moreover, ferric iron can also greatly affect where minerals plot on the quadrilateral, and the common procedure is to estimate ferric iron content based on simultaneous normalization of cations and charges.

The simplest projection procedure is to normalize Ca, Mg and Fe into 'Wo', 'En' and 'Fs' components:

$$\mathrm{Wo} = \mathrm{Ca}/(\mathrm{Ca}+\mathrm{Mg}+\mathrm{Fe})$$
$$\mathrm{En} = \mathrm{Mg}/(\mathrm{Ca}+\mathrm{Mg}+\mathrm{Fe})$$
$$\mathrm{Fs} = \mathrm{Fe}/(\mathrm{Ca}+\mathrm{Mg}+\mathrm{Fe}).$$

However, the non-quadrilateral components Ti, Al, $Fe^{3+}$ and $Cr^{3+}$ enter pyroxene by a Tschermak exchange (e.g. $AlAlMg_{-1}Si_{-1}$). A recalculation scheme that removes the Tschermak exchange would hold the Ca content of the pyroxene constant. Sodium enters pyroxene by the jadeite component along the exchange vector $NaAl^{6}Ca_{-1}Mg_{-1}$. Projection along this vector requires combining Ca + Na. A procedure that incorporates this thinking would first recalculate the pyroxene into end-members Wo, En + Fs, Cats and Jd, and then renormalize to Wo + En to obtain the quadrilateral Wo component:

$$\mathrm{Wo} = (\mathrm{Ca}+\mathrm{Na}-\mathrm{Al}^{6})/(\mathrm{Ca}+\mathrm{Na}-\mathrm{Al}^{6}+\mathrm{Mg})$$
$$\mathrm{En} = \mathrm{Mg}/(\mathrm{Ca}+\mathrm{Na}-\mathrm{Al}^{6}+\mathrm{Mg}).$$

In these formulae, $Al^{6}$ proxies for $Al^{6}+Fe^{3+}+Cr^{3+}+Ti$ and Mg proxies for Fe + Mg + Mn. En and Fs would be obtained by preservation of the Fe/(Fe + Mg) in the original pyroxene.

Neither of these projection schemes preserves the equilibrium implied by compositions of the original coexisting pyroxenes. For a simple example, let us consider the equilibrium between ortho- and clinopyroxene in the CMAS system (Fig. A1a). The pyroxenes can be described by the components enstatite ($Mg_2Si_2O_6$: En), Mg-Tschermak ($MgAlAlSiO_6$: Ts), and diopside ($CaMgSi_2O_6$: Di). At equilibrium, there are three linearly independent equilibrium relations that must be satisfied:

$$\mu_{\mathrm{en,opx}} = \mu_{\mathrm{en,cpx}}$$
$$\mu_{\mathrm{di,opx}} = \mu_{\mathrm{di,cpx}}$$
$$\mu_{\mathrm{ts,opx}} = \mu_{\mathrm{ts,cpx}}$$

for which the equilibrium constants are

$$K_{\mathrm{En}} = \frac{a_{\mathrm{en,\,cpx}}}{a_{\mathrm{en,\,opx}}} = \frac{[X_{\mathrm{Mg(M2)}}X_{\mathrm{Mg(M1)}}]_{\mathrm{cpx}}}{[X_{\mathrm{Mg(M2)}}X_{\mathrm{Mg(M1)}}]_{\mathrm{opx}}}$$

$$K_{\mathrm{En}} = \frac{a_{\mathrm{di,\,cpx}}}{a_{\mathrm{di,\,opx}}} = \frac{[X_{\mathrm{Ca(M2)}}X_{\mathrm{Mg(M1)}}]_{\mathrm{cpx}}}{[X_{\mathrm{Ca(M2)}}X_{\mathrm{Mg(M1)}}]_{\mathrm{opx}}}$$

$$K_{\mathrm{En}} = \frac{a_{\mathrm{ts,\,cpx}}}{a_{\mathrm{ts,\,opx}}} = \frac{[X_{\mathrm{Mg(M2)}}X_{\mathrm{Al(M1)}}]_{\mathrm{cpx}}}{[X_{\mathrm{Mg(M2)}}X_{\mathrm{Al(M1)}}]_{\mathrm{opx}}}$$

where ideal ionic activity models have been assumed and M1 and M2 refer to the crystallographic sites. These three equilibria define the entire set of two-phase opx + cpx tie lines (Fig. A1a). As can be seen from the graphical construction (Fig. A1a), the two-phase opx + cpx tie lines intersect the diopside–enstatite side line at points 'c', which is where an opx + cpx assemblage would plot in the Al-free system.

To find points 'c', the compositions of the coexisting pyroxenes for a specific assemblage are used to define the values of each $K_{\mathrm{eq}}$ for the assemblage. Using these same values for the equilibrium constant, these equations can then be solved again in the limit as Al(M1) approaches zero. There are eight unknowns [Mg(M2), Ca(M2), Mg(M1) and Al(M1) in each pyroxene]. In addition to the above constraints, the constraints

$$\mathrm{Ca(M2)} + \mathrm{Mg(M2)} = 1$$
$$\mathrm{Mg(M1)} + \mathrm{Al(M1)} = 1$$

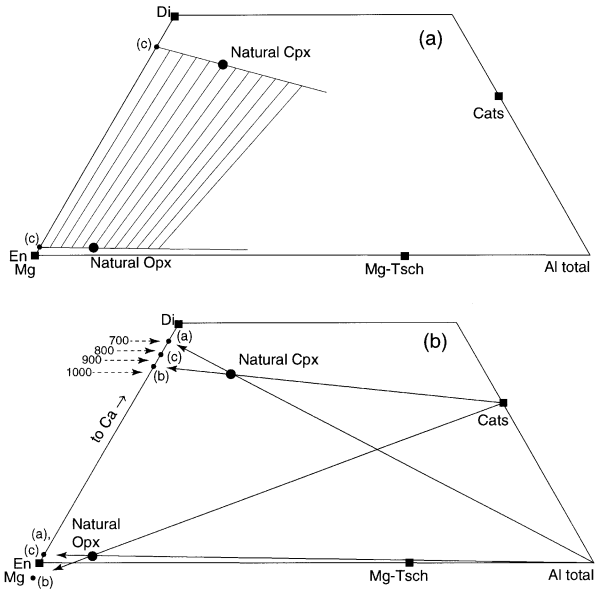


**Fig. A1.** (a) AC(FM) diagram showing the graphical basis of the 'thermodynamic projection' scheme used to project from non-quadrilateral components onto the pyroxene quadrilateral. Large dots are a representative opx + cpx assemblage. Schematic tie lines are shown to define the two-phase opx + cpx region. Points 'c' are the intersection of the two-phase region with the Al-free diopside–enstatite join. (b) AC(FM) diagram showing the effect of different projection schemes on plotting positions of pyroxenes on the pyroxene quadrilateral (diopside–enstatite join). The original ortho- and clinopyroxenes contain 0·08 and 0·14 cations/6 oxygens of $Al + Ti + Fe^{3+}$, respectively. Projection point 'a' is from the simple normalization scheme. Projection point 'b' projects along exchange vectors. Projection point 'c' results from a thermodynamic projection (Spear, 1988). Temperatures shown reflect isotherms for coexisting ortho- and clinopyroxene at Fe/(Fe + Mg) = 0·4 from Sack & Ghiorso (1994). (Note that the temperatures inferred from the three projection schemes each differ by 125°C.) Di, diopside; En, enstatite; Cats, Ca-Tschermaks; Mg-Tsch, Mg-Tschermaks.

*Table A1: Model calculation for projection schemes onto pyroxene quadrilateral*

| | Opx | Cpx |
|---|---|---|
| *Compositions* | | |
| Si | 1·91 | 1·85 |
| $Al^4$ | 0·09 | 0·15 |
| Al(M1) | 0·09 | 0·15 |
| Mg(M1) | 0·91 | 0·85 |
| Mg(M2) | 0·98 | 0·15 |
| Ca(M2) | 0·02 | 0·85 |
| *Simple normalization* | | |
| Wo | 0·010 | 0·460 |
| En | 0·990 | 0·540 |
| *Projection along exchange vectors* | | |
| Wo | −0·038 | 0·412 |
| En | 1·038 | 0·588 |
| *Thermodynamic projection* | | |
| Wo | 0·012 | 0·435 |
| En | 0·988 | 0·565 |

also apply for each pyroxene, leaving seven equations in eight unknowns. The equations can therefore be solved by setting the value of a single variable, namely the value of Al(M1). Setting Al(M1) to a very small number (effectively zero), the resulting solution will be point 'c'.

This approach was described as a 'thermodynamic projection' by Spear (1988), where it was developed for projecting pelites onto the AFM diagram of Thompson (1957). The approach may be generalized to any number of phases and components, and incorporate any solutions model. If Na is present, there is one extra equation (the equilibrium for jadeite component between the two pyroxenes) and two additional unknowns (the Na content of each pyroxene), so solutions require also setting $X_{Na} \sim 0$. The addition of Fe to the system requires setting the value of the ordering parameter [Fe(M1)–Fe(M2)] in one pyroxene to a constant (this is appropriate so long as ordering is not a function of Al content). Solution of the above set of equations requires solution to a set of linear and non-linear equations. An alternative approach [and the one used computationally by Spear (1988)] is to use the differential thermodynamics approach known as the Gibbs method (Spear *et al.*, 1982; Spear, 1989), which uses the differentials of the above equations (which are linear) and solves them iteratively using a finite difference scheme as $X_{Al(M1)}$ approaches zero.

As an example, the three sets of recalculations have been performed on the pair of pyroxenes shown in Table A1 and plotted in Fig. A1b. These compositions were chosen as representative of the amounts of $Al + Ti + Fe^{3+}$ in the present suite of pyroxenes. For clinopyroxene, the simple normalization results in the largest Wo component in clinopyroxene, whereas the exchange vector projection results in the lowest. The thermodynamic projection plots at intermediate Wo contents. For orthopyroxene, the simple normalization and thermodynamic projections plot at nearly identical points, whereas the exchange vector projection plots at negative Wo component owing to the excess of $Al^6$ over Ca.

It is illustrative to consider the effect of these recalculations on temperatures estimated from pyroxene thermometry. The 700, 800, 900 and 1000°C isotherms of Sack & Ghiorso (1994) [projected onto an Fe/(Fe + Mg) of 0·4] are shown along the Ca–Mg sideline of the plot in Fig. A1b. The simple normalization, exchange

vector projection and thermodynamic projection schemes record apparent temperatures of 700, 950 and 825°C, respectively. The large difference among these three inferred temperatures underscores the need for an appropriate recalculation scheme for pyroxenes.

## APPENDIX B: THERMOCHEMICAL DATA AND ACTIVITY MODELS

Standard state thermodynamic data for phases quartz, plagioclase, garnet, orthopyroxene and clinopyroxene have been taken from Berman (1988, 1990). Where entropy and volume data for end-members were not available in Berman's database, exchange heat capacities, entropies, and volumes have been calculated using equations of Berman & Brown (1985) and Holland (1989), respectively. Plagioclase solution properties are assumed to be ideal, and activities of garnet components follow Berman (1990).

Orthopyroxene and clinopyroxene have been modeled as multi-site crystals with the general formula $(M2)(M1)T_2O_6$. Site assignments are made as follows: (1) all Si is assigned to tetrahedral coordination; (2) sufficient Al is assigned to tetrahedral coordination to make $Si+Al^4=2$ with the remainder of the Al assigned to M1; (3) Fe and Mg are partitioned between M1 and M2 using ordering energies given by Sack & Ghiorso (1994); (4) all Ca and Na is assigned to M2. With these site assignments, an ideal ionic mixing model was found to reproduce qualitatively the experimental data of Harley (1984*b*) for the assemblage orthopyroxene + garnet + quartz in the FMAS system. Following Harley (1984*b*), addition of an excess parameter for Fe–Al mixing on the M1 site (30 000 J/mol in this study) was found to reproduce the experimental data fairly well. Although inadequate for prediction of phase equilibria in pyroxene-bearing systems, the simplified solution models introduce errors of <1% over the range of compositional zoning encountered in this study.